

Tree-based solvers for adaptive mesh refinement code FLASH - III: a novel scheme for radiation pressure on dust and gas and radiative transfer from diffuse sources.

A. Klepitko¹^{*}, S. Walch^{1,2}[†], R. Wünsch³, D. Seifried^{1,2},
F. Dinnbier⁴, S. Haid¹

¹*Physikalisches Institut, Universität zu Köln, Zùlpicher Str. 77, 50937 Köln, Germany*

²*Center for data and simulation science, University of Cologne, www.cds.uni-koeln.de*

³*Astronomical Institute, Academy of Sciences of the Czech Republic, Bocni II 1401, 141 31 Prague, Czech Republic*

⁴*Astronomical Institute, Faculty of Mathematics and Physics, Charles University, V Holešovičkách 2, 180 00 Praha 8, Czech Republic*

Accepted XXX. Received YYY; in original form ZZZ

ABSTRACT

Radiation is an important contributor to the energetics of the interstellar medium, yet its transport is difficult to solve numerically. We present a novel approach towards solving radiative transfer of diffuse sources via backwards ray tracing. Here we focus on the radiative transfer of infrared radiation and the radiation pressure on dust. The new module, TREERAY/RADPRESSURE, is an extension to the novel radiative transfer method TREERAY implemented in the grid-based MHD code FLASH. In TREERAY/RADPRESSURE, every cell and every star particle is a source of infrared radiation. We also describe how gas, dust and radiation are coupled via a chemical network. This allows us to compute the local dust temperature in thermal equilibrium, leading to a significantly improvement over the classical grey approximation. In several tests, we demonstrate that the scheme produces the correct radiative intensities as well as the correct momentum input by radiation pressure. Subsequently, we apply our new scheme to model massive star formation from a collapsing, turbulent core of 150 M_{\odot} . We trace the effects of both, ionizing and infrared radiation on the dynamics of the core. We find that the newborn massive star(s) prevent fragmentation in their proximity through radiative heating. Over time, dust and radiation temperature equalize, while the gas temperature can be either warmer due to shock heating or colder due to insufficient dust-gas coupling. Compared to gravity, the effects of radiation pressure become significant on the core scale only at an evolved stage.

Key words: radiative transfer – radiation hydrodynamics – backwards ray tracing – dust cooling – massive star formation

1 INTRODUCTION

Radiation provides a channel through which energy and momentum may be transported independently from the flow of mass. This makes it an integral part of the physical processes of the interstellar medium (ISM). The impact of radiation ranges from peaceful processes such as line emission cooling, continuum radiation cooling and heating – to violently driven HII regions (Spitzer 1978) and radiation pressure (RP) driven outflows. This enables radiative processes to regulate the star formation efficiency both ways – increasing it through cooling processes, enabling gas to col-

lapse, and decreasing it through explosive expansion resulting in the removal of gas. Especially in recent works, RP is discussed as a mechanism to limit star formation. Matzner (2002) argues that giant molecular clouds are supported by the feedback of their most massive stars. Sites of massive star formation are those with column densities greater than 0.1 g cm^{-2} (Tan et al. 2014). Thompson et al. (2005) discuss the importance of RP on galactic scales and argue that RP from dust acts as an anti-catalyst for the star formation rate in ultra-luminous infrared galaxies.

The combination of photoionization and RP is discussed by Kuiper & Hosokawa (2018) in the context of massive star formation, where they find that RP plays a role at later stages and may limit the final mass of a massive star. Rosen et al. (2019) find that RP may lead to cavities, which only

^{*} E-mail: klepitko@ph1.uni-koeln.de

[†] E-mail: walch@ph1.uni-koeln.de

allow for disk accretion onto the star at later stages. Eventually the mass flow onto the disk is cut off resulting in starvation of the disk and limiting the total accretion onto the star.

Solving radiative transfer (RT) numerically is difficult to accomplish, because RT can be considered a non-local problem to solve in the context of hydrodynamical simulations. This makes solving RT to a certain degree similar to the problem of solving gravity, where its numerical solution requires a lot of communication. However, unlike gravity, radiation may be shielded or reprocessed, rendering the problem even more difficult than solving gravity numerically. Recent improvements in computer hardware, ever-growing supercomputers, and the development of numerical methods enabled RT to be treated on the fly in state-of-the-art numerical simulations. [Bisbas et al. \(2015\)](#) show benchmarks of 11 independent approaches towards solving the D-type expansion of an HII region driven by a single source. This highlights the effort that is put into solving RT in current numerical codes.

The pioneering work of [Levermore & Pomraning \(1981\)](#) formulates a flux-limited diffusion (FLD) theory, of which core concepts are still used in state-of-the-art numerical simulations and codes today (e.g. [Krumholz et al. 2007](#); [Kuiper & Hosokawa 2018](#), and many others). Here, radiation is treated in the form of an energy density and evolved according to the diffusion equation. This formalism transforms RT into a local problem, which is beneficial from a computational perspective as very little communication is required during the computation. As a trade-off the timestep is limited through the speed of light. This limitation can be partially overcome in a reduced speed of light approximation.

M1 closure builds on the FLD method and introduces more accuracy to the solution by taking into account one more moment to advect its radiation energy density. This leads to M1 closure capturing shadows more accurate than FLD ([Levermore 1984](#); [Rosdahl & Teyssier 2015](#); [Kannan et al. 2019](#)). However, M1 closure may result in colliding flows of radiation if multiple sources are present ([Menon et al. 2022](#)). The work of [Menon et al. \(2022\)](#) employs a variable Eddington tensor method which greatly improves the result of the radiation field. Their algorithm, VETTAM, uses ray-tracing to compute the variable Eddington tensor in a hybrid characteristics approach.

A different approach to solving RT is ray tracing, where multiple rays are cast to probe the environment along different lines of sight. Ray tracing yields more accurate results in terms of shadow casting than moment methods. This is especially the case if the radiation originates from many pointlike sources, with the trade-off of being computationally more demanding compared to moment methods or FLD. Examples of ray tracing can be found in the works of [Baczynski et al. \(2015\)](#) and also [Kim et al. \(2018\)](#) where they solve the forward propagation of ionizing radiation based on the methods of [Abel & Wandelt \(2002\)](#). Forward ray tracing (FRT) may quickly become infeasible if the number of sources grows, limiting the applicability of FRT. For this reason FRT is not suited for modelling reprocessed radiation, because of the sheer number of sources involved i.e. each gaseous or dusty cell can be a source of radiation. [Rosen et al. \(2017\)](#) and [Kuiper et al. \(2020\)](#) use a hybrid solution where radiation originating from pointlike sources is

modelled with FRT while the reprocessed radiation is modelled with FLD. The early work of [Kessel-Deynet & Burkert \(2000\)](#) shows a different approach to ray tracing, where they use backwards ray tracing to solve RT of ionizing radiation. Another example can be found in the work of [Grond et al. \(2019\)](#) where a single ray from each point in space is cast to every source of radiation along which RT is solved. Their approach, named TREVR, merges sources and adaptively refines on extinguishing material to save on computational effort. Over all, TREVR scales with an $(N \log^2(N))$ relation. Following this approach calculations on taking into account emission from dust may become infeasible.

[Wünsch et al. \(2018\)](#) solve gravity in adaptive mesh refinement (AMR) simulations with a tree-solver operating on an octal-spatial tree (Octtree). In a next step, [Wünsch et al. \(2021\)](#) expand the method to treat ionizing radiation from pointlike sources in a backwards ray tracing approach, called TREERAY/ONTHESPOT. This work will build on both these papers and will expand the applicability of TREERAY to treat reprocessed radiation from dust. Or more general, this work will explore solving radiative transfer from macroscopic sources via backwards ray tracing.

This work discusses three types of radiation: ionising radiation from point sources (e.g. stars), non-ionising radiation from point sources, and non-ionising radiation from dust. The transport of the first one is treated by the TREERAY/ONTHESPOT module described in [Wünsch et al. \(2021\)](#), calculating its absorption by gas through the case B recombination and the gas heating. Here, we add the interaction of ionising radiation with dust, specifically, its radiation pressure on dust and gas. The absorption of ionising radiation by dust is neglected. The TREERAY/RADPRESSURE module described here calculates the transport of the non-ionising radiation from point sources and from dust. Both types of the non-ionising radiation interact directly only with the dust. In the latter we assume that dust and gas are always dynamically coupled and the momentum inserted by the radiation pressure to the dust is immediately transferred to the gas.

This manuscript is structured as follows. In §2 we recall basics and simplifications on radiative transfer relevant to this work. In §3 we summarize the numerical methods used in this work followed by a detailed explanation of the novel radiative transfer scheme given in §4. We show tests verifying the correctness of the scheme in §5. We follow this up with two more sophisticated setups covering the expansion of an HII region in §6 and a star forming setup in §7.

2 SIMPLE, DUSTY RADIATIVE TRANSFER

In this section we briefly define the essentials of radiative transfer while focussing on dust. We employ simplifications to aid the speedup of the algorithm.

The radiative transfer equation for the frequency-dependent radiation intensity, I_ν , propagating along a unit vector, $\hat{\mathbf{n}}$, reads

$$\left(\frac{1}{c} \frac{\partial}{\partial t} + \hat{\mathbf{n}} \cdot \nabla\right) I_\nu = -a_\nu I_\nu + j_\nu, \quad (1)$$

where t , ν , a_ν and j_ν are the unit time, the frequency of the light and the extinction and emission coefficient, respectively ([Mihalas & Mihalas 2013](#)). In the following we will

assume c to approach infinity in eq. 1. As a consequence, contributions from the time derivative vanish, such that one arrives at an equilibrium solution. By doing this, we can not model the propagation of light within a small time window dt accurately. However, given that the sound crossing time is much larger than the light crossing time on astrophysical scales, this is a reasonable approximation. Further we drop all frequency dependencies by introducing a Planck weighting.

By doing so we arrive at a formulation of eq. 1 that is greatly simplified, namely

$$\hat{\mathbf{n}} \cdot \nabla I = -aI + j, \quad (2)$$

where a and j are the Planck-weighted mean extinction and emission coefficient, respectively, and I is the total radiation intensity. We summarize

$$I = \int_0^\infty I_\nu d\nu, \quad (3)$$

$$a = \kappa_P \rho, \quad (4)$$

$$j = \frac{\sigma}{\pi} \kappa_P \rho T^4, \quad (5)$$

$$\kappa_P = \frac{\int_0^\infty \kappa_\nu B_\nu d\nu}{\int_0^\infty B_\nu d\nu}, \quad (6)$$

where κ_P is the Planck mean opacity. Throughout this work, we employ the Planck mean dust opacity based on [Semenov et al. \(2003\)](#). The model description we choose is the same as stated by [Krumholz & Thompson \(2012\)](#):

$$\kappa_P(T) = 10^{-1} \frac{\text{cm}^2}{100 \text{ K}^2 \text{ g}} \times \begin{cases} T^2 & \text{for } T < 150 \text{ K} \\ 150^2 & \text{else} \end{cases}. \quad (7)$$

In the following we drop the index P such that $\kappa := \kappa_P$.

We define the radiative flux, \mathbf{F} , and the mean radiative intensity, \bar{J} , in the following way

$$\mathbf{F} = - \oint_S I \hat{\mathbf{n}}_{\text{rad}} d\Omega, \quad (8)$$

$$\bar{J} = \frac{1}{4\pi} \oint_S I d\Omega. \quad (9)$$

Here, $\hat{\mathbf{n}}_{\text{rad}}$ is the radial unit vector pointing from the origin towards the surface of a unit sphere, S , and $d\Omega$ is the solid angle around $\hat{\mathbf{n}}_{\text{rad}}$.

2.1 Effective area of an infinitesimal volume of dust

In this section we discuss the emission properties of dust in the context of three-dimensional emission. In the following, we argue that the effective area, dA , from which dust inside an infinitesimal volume, dV of mass density ρ emits radiation into a solid angle $d\Omega$, is given by

$$\cos \vartheta dA d\Omega = \kappa \rho dV d\Omega, \quad (10)$$

where ϑ is the angle between the surface normal of dA and solid angle $d\Omega$.

Following Eq. 2, the decrease in radiation intensity as a function of distance from the radiation source is governed by the extinction coefficient. Both the effects of scattering and absorption contribute to a . If we neglect scattering, we can express a as the product of the mass density and the

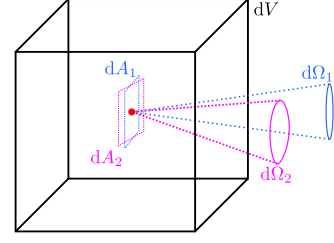


Figure 1. Schematic picture of an infinitesimal volume, dV , from which radiation is emitted into solid angles, $d\Omega_1$ and $d\Omega_2$. The associated areas of the solid angles, $d\Omega_1$ and $d\Omega_2$, are labeled dA_1 and dA_2 , respectively. The relation $|dA_1| = |dA_2|$ holds. The source radiates with $L_\Omega^0 = \frac{\sigma}{\pi} \rho \kappa T^4$ into every solid angle (see Eq. 13).

dust opacity (Eq. 4). Following its dimensionality, $L^2 M^{-1}$, the dust opacity can be understood as an associated area per unit mass. It is the effective area through which dust interacts with radiation.

For the cubic, infinitesimal volume, $dV = (dr)^3$, filled with material of mass density ρ , we can express the contained mass as $dm = \rho dV$. A one-dimensional ray penetrating dV and traveling through its length, dr , would act on an area $dA = \kappa dm = \kappa \rho dV = (dr)^2 (\kappa \rho dr)$. The last term

$$\tau = \kappa \rho dr \quad (11)$$

represents the optical depth, τ , through the volume element. Here, in this instance, we only consider volumes which are so small that they are certainly optically thin (in the numerical implementation we separately treat optically thin and thick volumes; see §4).

At the same time, dA is the effective area from which thermal radiation is emitted by the volume into the path of the ray. Note, that dA is invariant under rotation, since the spatial distribution of dust within dV is assumed to be homogeneous (i.e. $|dA_1| = |dA_2| =: dA$ in Fig. 1). For this reason, dV emits and absorbs radiation isotropically. Because of the isotropic emission behaviour of such a volume of dust, we can neglect the $\cos \vartheta$ factor as there always exists an area dA which is normal to a chosen $d\Omega$. This yields $\vartheta = 0$ and therefore $\cos \vartheta = 1$.

2.2 Thermal emission of an infinitesimal volume

We model the radiation of dust to be of thermal nature. Let $L_\Omega^0(T) \cos \vartheta dA d\Omega$ measure the luminosity of thermal radiation emitted from an effective surface element, dA , at temperature T into a solid angle $d\Omega$. The following equation holds ([Mihalas & Mihalas 2013](#)):

$$L_\Omega^0(T) \cos \vartheta dA d\Omega = \frac{\sigma}{\pi} T^4 \cos \vartheta dA d\Omega. \quad (12)$$

Combining eq. 10 and eq. 12 yields

$$L_\Omega^0(T) \kappa \rho dV d\Omega = \frac{\sigma}{\pi} \kappa \rho T^4 dV d\Omega, \quad (13)$$

where σ is the Stefan-Boltzmann constant. Fig. 1 schematically shows how an area dA_1 represents a fraction of the surface area of dV .

Since we aim to model radiative transfer from dust and we assume the dust to be distributed smoothly within dV , we can use dA to model the emission from a small volume dV .

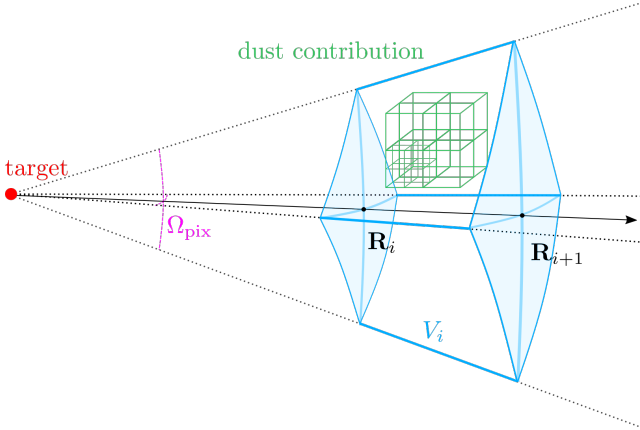


Figure 2. Graphical representation of a single HEALPIX ray. The ray is of angular size Ω_{pix} (pink) and has multiple evaluation points along its radial direction. One such evaluation point is labeled with i and has an associated distance \mathbf{R}_i from the target point (black dot). The volume V_i (blue) associated with evaluation point i is bound by \mathbf{R}_i and \mathbf{R}_{i+1} in radial direction. The dust contributions (green) exist on an octree structure and can be mapped to rays adaptively.

3 NUMERICAL METHODS

We use the highly scalable code FLASH 4.3 (Fryxell et al. 2000) to solve the ideal hydrodynamics equations with gravity (Wünsch et al. 2018), ionizing radiation (Wünsch et al. 2021) and non-ionizing radiation. For the first time we present results from our backwards ray tracing infrared radiative transfer method, TREERAY/RADPRESSURE, implemented in FLASH4.3¹.

TREERAY/RADPRESSURE allows to compute radiation fields from both pointlike (e.g. stars represented by sink particles) and macroscopic sources (e.g. radiation from dust) taking into account absorption and emission on the fly. The latter is accomplished by allowing for every cell to be a source. With the radiation fields at hand we can treat the effects of radiation pressure and radiative heating and cooling through dust. We explain the details of TREERAY/RADPRESSURE in section 4 and how we treat heating and cooling of gas through dust in section 4.6. Before, we introduce point sources in the form of sink particles to model star formation and its arising feedback self-consistently (see §3.1). We make use of a sub-grid model to compute both the emitted ionising and non-ionising radiation.

3.1 Sink particles

Our implementation of sink particles is based on the implementation of Dinbier & Walch (2020) in the FLASH code. Which basically follows the the algorithm of Federrath et al. (2010) for sink formation and accretion (see below), but the integrator is a 4th order Hermite scheme and the method is coupled to the gravity tree in order to evaluate gas-sink interactions.

All volumes, V_{sink} , which have a density greater than ρ_{thresh} qualify to form sink particles. We set ρ_{thresh} to be the Jeans density for a Jeans length corresponding to 4 grid cell sizes at highest refinement, fulfilling the conditions of Truelove et al. (1997). Additionally, we allow for the formation of a sink particle inside V_{sink} if and only if all of the following conditions are met:

- (i) V_{sink} is on maximum refinement,
- (ii) V_{sink} is free of sink particles,
- (iii) gas inside V_{sink} is infalling,
- (iv) V_{sink} is located on a gravitational potential minimum,
- (v) gas inside V_{sink} is gravitationally bound,
- (vi) gas inside V_{sink} will collapse within its own free fall time before it has the chance of being accreted by another sink particle (see Clarke et al. (2017), their eq. 4 and 5).

Conditions (i) to (v) are taken from Federrath et al. (2010) and condition (vi) has been taken from Clarke et al. (2017). We find that (vi) substantially reduces the number of sinks formed in accordance with Clarke et al. (2017).

We allow sink particles to model protostellar cores, where we use the implementation of Klassen et al. (2012) on GitHub². From the model we obtain an internal luminosity, L_{int} , as well as an accretion luminosity, L_{acc} . We assign each of these luminosities, L_{int} and L_{acc} , a temperature, T_{int} and T_{acc} , respectively, in the following way

$$T_{\text{int}} = \left(\frac{L_{\text{int}}}{\sigma 4\pi r_{\text{star}}^2} \right)^{1/4}, \quad (14)$$

$$T_{\text{acc}} = \left(\frac{L_{\text{acc}}}{f_{\text{filling}} \sigma 4\pi r_{\text{star}}^2} \right)^{1/4}, \quad (15)$$

where r_{star} and f_{filling} are the stellar radius and the fraction of the area of the star upon which the star is accreting. We obtain r_{star} from the protostellar model and set $f_{\text{filling}} = 0.1$ (Calvet & Gullbring 1998). Finally we split each luminosity, L_X (where $X = \text{int}$ or $X = \text{acc}$, based on its temperature, T_X , to contribute towards ionizing radiation with a fraction, $\gamma(T_X)$, and its complement, $(1 - \gamma(T_X))$, to contribute towards non ionizing radiation. We compute the fraction $\gamma(T_X)$ by computing the ratio of luminosity emitted in the Lyman band and the bolometric luminosity at temperature T_X . This is computed as such

$$\gamma(T_X) = \frac{\int_{\nu_{\text{LyC}}}^{\infty} d\nu B_\nu(T_X)}{\int_0^{\infty} d\nu B_\nu(T_X)}, \quad (16)$$

where ν_{LyC} marks the lower frequency of the Lyman continuum, and B_ν is Planck's law of black body radiation.

In total one can state the ionizing luminosity, $L_{\text{src, UV}}$, and the non-ionizing luminosity, $L_{\text{src, IR}}$, of a sink particle as:

$$L_{\text{src, UV}} = \gamma(T_{\text{int}})L_{\text{int}} + \gamma(T_{\text{acc}})L_{\text{acc}}, \quad (17)$$

$$L_{\text{src, IR}} = L_{\text{int}} + L_{\text{acc}} - L_{\text{src, UV}}. \quad (18)$$

We discuss the treatment of the non ionizing luminosity, $L_{\text{src, IR}}$, in this work and treat the ionizing luminosity, $L_{\text{src, UV}}$, as discussed by Wünsch et al. (2021).

¹ The method has been transferred to FLASH4.6 as well.

² https://github.com/mikhailklassen/protostellar_evolution

4 RADIATIVE TRANSFER ALGORITHM

The algorithm presented in this work builds on TREERAY (Wünsch et al. 2021) as a framework. The general approach uses backwards ray tracing to solve radiative transfer. For the algorithm to work efficiently, it is necessary that the information of the computational domain is stored in a volume dividing tree. To do this, we employ an octree in the current implementation. From each point of interest we cast rays aligned with the pixel defined by the HEALPIX algorithm (Górski et al. 2005). Fig. 2 illustrates the shape and components of a ray originating from a point of interest (target position, red dot). For each ray we map contributions to the ray based on their geometric intersection. The contributions are mapped on a node basis, as they naturally occur in an oct-tree. If the nodes appear larger than an angle, θ_{lim} , while being mapped to a ray, they are rejected and opened instead. This refinement process is repeated until we eventually reach leaves of the tree, in which case they are guaranteed to be accepted. In a final step we integrate the rays to obtain useful quantities. In our case we focus on dust, a macroscopic source potentially permeating the entire computational domain. Applications of TREERAY solving radiative transfer for ionizing radiation can be found in the works of Haid et al. (2018), Haid et al. (2019) and Dinmbier & Walch (2020).

In the general spirit of TREERAY, we will solve radiative transfer for infrared radiation with backwards ray tracing. The method consists of multiple conceptual parts: (1) we save necessary quantities on the tree (see §4.1); (2) we cast rays from our target point in order to probe the surroundings, tree-nodes are mapped to the rays (see §4.2); (3) we integrate individual rays (see §4.3); (4) perform final calculations after knowing results from all rays (see §4.4). In §4.5 we compute the momentum from our flux. The additional features presented in this work recover the same computational strong and weak scaling as presented in the work of Wünsch et al. (2021) in terms of their performance that is $N \log(N)$.

The main goals of this module are to calculate both the acceleration caused by RP, \mathbf{a}_{RP} , projected onto the cartesian coordinates x , y , and z as well as the radiation intensity, J . The accelerations are stored in 3 fields within FLASH named RPAX, RPAY and RPAZ and have units cm s^{-2} each. We explain the calculation of \mathbf{a}_{RP} starting in §4.1 and arrive at the final expression in §4.5. The calculation of the mean radiative intensity, J , which is stored in the field variable IRXE of units $\text{erg s}^{-1} \text{cm}^{-2} \text{sr}^{-1}$, is finalized in section §4.4. The directly trapped radiation pressure, P_{src} , is stored in the field PRAD and has the units dyn cm^{-2} . We use this quantity to account for RP due to direct absorption of radiation within a cell. The dust temperature, T_{dust} , is stored in the field TDUS with units K.

Due to the difference of radiation being emitted from an optically thin volume compared to that of an optically thick volume, we need to treat either case inherently separate. While optically thin material can radiate from its entire volume, optically thick material can only radiate from its surface. Since we use backwards ray tracing that adaptively refines the grid, we need to make simplifications, as the exact geometry of the material is unknown. For our simplifications we assume a complete mixing for the optically thin material and assume a compact geometry for optically

thick material at given radial distances for the entire solid angle of the rays.

4.1 Tree build

Information about regions in space are stored in an oct-tree structure. We use the term *node* whenever we talk about data stored inside the tree. Nodes representing the AMR grid at the locally highest refinement are referred to as *bottom nodes* ($:=$ *b-node*). *Higher level nodes* ($:=$ *h-node*) are all nodes which are not bottom nodes.

4.1.1 Bottom nodes

We store different quantities on a b-node depending on the b-node being optically thin or thick. A node is labeled optically thin if its optical depth, $\tau_{\text{b-node}}$, is less than 1 and optically thick otherwise. We calculate $\tau_{\text{b-node}}$ for our nodes of cubic shape with volume $dV = dr^3$ as such:

$$\tau_{\text{b-node}} = \rho \kappa dr. \quad (19)$$

For an optically thin node we store:

$$L_{\text{b-node, thin}} = 4\sigma\rho\kappa(T_{\text{dust}})^4 dV, \quad (20)$$

$$\tilde{A}_{\text{b-node}} = \rho \kappa dV, \quad (21)$$

$$S_{\text{b-node}} = L_{\text{src, IR}} \times e^{-\tau_{\text{b-node}}/2}, \quad (22)$$

where $L_{\text{b-node, thin}}$ is the optically thin luminosity of the node and \tilde{A} is the associated area, $S_{\text{b-node}}$ are luminosity contributions from pointlike sources like sink particles. L_{src} is the non ionizing luminosity of pointlike particles present in a bottom node (see eq. 18). The complement of the pointlike sources contributions is used to heat the node and added as a trapped radiation pressure. \tilde{A} can be interpreted as an associated area for a volume to interact with radiation analogue to the concept discussed in §2.1. Fig. 1 shows the associated area of an optically thin volume. Later on \tilde{A} will be used to compute extinction along the ray.

For an optically thick node we store:

$$\underline{L}_{\text{b-node, thick}} = \frac{\sigma}{\pi}(T_{\text{dust}})^4, \quad (23)$$

$\tilde{A}_{\text{b-node}}$ and $S_{\text{b-node}}$, where $\underline{L}_{\text{b-node, thick}}$ is the luminosity per area emitted from a solid black body into a solid angle. Note that we indicate the different units between the luminosities stored on optically thin and thick nodes by an underline (compare Eq. 20 and Eq. 23). In our implementation we toggle the bit responsible for storing the \pm -sign of $L_{\text{b-node}}$ in the memory to indicate whether a node is optically thin or thick on the bottom layer. By doing this we keep the memory footprint of the bottom nodes small by containing only 3 floats. This enhancement is doable because a negative luminosity is not meaningful in our scheme.

4.1.2 Higher level nodes

Higher level nodes are created by joining 8 subvolumina together into a bigger volume. We refer to a subvolume of a higher level node as a *sub-node*. The edge length of a node is twice that of its sub-node in our implementation.

We propagate the information from the bottom of the

tree upwards to each h-node by summation over all sub-nodes. The details can be found in §A of the appendix. The quantities are stored separately for optically thin and thick material in h-nodes, so that we can trace the optically thin and thick content of L , \hat{A} and V inside each h-node.

Each of the h-nodes holds \mathbf{r}_{COL} pointing from the geometric center of the h-node to its center of luminosity (COL). We find that taking into account \mathbf{r}_{COL} while mapping nodes helps improving errors introduced by coarsening at greater distances. Again the details can be found in §A of the appendix.

4.2 Ray mapping

Each target is equipped with a set of rays defined by the pixels generated by the HEALPIX algorithm (Górski et al. 2005). We will distinguish the rays with the index h . The total number of rays is given by N_{pix} . Note that each cell in our computation is considered to be a target point.

A single ray has multiple evaluation points along its direction, which will be labeled with the index i . Their spacing from the target, \mathbf{R}_i , grows quadratically. We choose this spacing because it is on par with the angular resolution criterion, where we satisfy that nodes are opened until they appear to be smaller than a certain angle. A more detailed discussion can be found in the work of Wünsch et al. (2021). The volume, V_i , associated with evaluation point i is the space between evaluation point i and $i+1$. Fig. 2 illustrates the shape of a ray and all the quantities just mentioned.

Two kernels in the form of lookup tables are used in order to map nodes to rays. First, the angular overlapping fraction, $\alpha_{\text{node}}(h)$, of a node with a ray, h , is looked up in the corresponding kernel. The kernel holds monte-carlo precalculated values for nodes of different node sizes at discrete angles, $\vartheta_{\text{fine},j}$ and $\varphi_{\text{fine},j}$, and discrete distances, $R_{\text{fine},j}$. These discrete coordinates are chosen such that they closely represent the true position of the node (i.e. by taking the closest matching discrete value for either value). The second kernel treats radial mapping. It ensures that quantities affected by the inverse square law stay conserved, when they are mapped from their true position, \mathbf{r}_{node} , to an evaluation point at distance R_i . The kernel holds pre-calculated correction values for nodes at discrete distances $R_{\text{fine},j}$. By choosing a large set of $R_{\text{fine},j}$ we approximate the true correction factor, $\beta_{\text{node}}^*(i)$, with, $\beta_{\text{node}}(i)$, such that

$$\beta_{\text{node}}(i) = \frac{R_{\text{fine},j}^2}{R_i^2} \approx \frac{r_{\text{node}}^2}{R_i^2} = \beta_{\text{node}}^*(i). \quad (24)$$

For a given node at distance r_{node} , $R_{\text{fine},j}$ is chosen so that

$$(R_{\text{fine},j} < r_{\text{node}}) \wedge (R_{\text{fine},j+1} > r_{\text{node}}) \quad (25)$$

hold. We allocate the radial kernel inside shared memory, because of its large size. This allows us to keep the memory footprint small while allowing for great precision.

4.2.1 Optically thin nodes

We correct inverse square law sensitive quantities in the following way:

$$\hat{L}_{\text{node}} = \beta_{\text{node}} L_{\text{node}}, \quad (26)$$

$$\hat{A}_{\text{node}} = \beta_{\text{node}} \tilde{A}_{\text{node}}. \quad (27)$$

This way the flux seen from the luminosity \hat{L}_{node} at distance R_i approximates the flux seen from L_{node} at distance r_{node} . The same holds for \hat{A}_{node} .

Each evaluation point, i , of a ray, h , holds

$$\hat{L}_{\text{thin},i}^h = \sum_{\text{nodes}(i)} \alpha_{\text{node}}(h) \hat{L}_{\text{node,thin}}, \quad (28)$$

$$\hat{A}_{\text{thin},i}^h = \sum_{\text{nodes}(i)} \alpha_{\text{node}}(h) \hat{A}_{\text{node}}, \quad (29)$$

$$\hat{V}_{\text{thin},i}^h = \sum_{\text{nodes}(i)} \alpha_{\text{node}}(h) V_{\text{node}}, \quad (30)$$

where $\text{nodes}(i)$ describes the set of nodes mapped to evaluation point i . \hat{L}_i^h can be understood as the total unextincted luminosity of segment i of ray h . In section 4.3 we will use \hat{A}_i^h to compute the corrected luminosity of our segment i . V_{node} is the volume of the node volume (which is known).

4.2.2 Optically thick nodes

For optically thick nodes we map the following quantities to rays:

$$\hat{L}_{\text{thick},i}^h = \sum_{\text{nodes}(i)} \alpha_{\text{node}}(h) \underline{L}_{\text{node,thick}} V_{\text{node}}, \quad (31)$$

$$\hat{A}_{\text{thick},i}^h = \sum_{\text{nodes}(i)} A_{\text{node}}, \quad (32)$$

$$\hat{V}_{\text{thick},i}^h = \sum_{\text{nodes}(i)} \alpha_{\text{node}}(h) V_{\text{node}}, \quad (33)$$

$$\hat{Q}_{\text{thick},i}^h = \sum_{\text{nodes}(i)} \alpha_{\text{node}}(h) \beta_{\text{node}}(i) V_{\text{node}}. \quad (34)$$

Similar to eq. 28, 29 and 30 in the optically thin case we map the luminosity, area and volume in the optically thick case as well. A fourth quantity is mapped, $\hat{Q}_{\text{thick},i}^h$, which will later on be used to compute the angular size of the optically thick material. $\hat{Q}_{\text{thick},i}^h$ is the only quantity that holds information about the inverse square law corrections concerning the treatment of optically thick nodes.

4.3 Ray integration

In the following we will benefit from eq. 2 being 1 dimensional and aligned with our radial direction. We will apply eq. 2 to integrate each ray individually from the inside out. For each ray segment, i , along a pixel, h , we will compute extinction (see section 4.3.1) and emission (see section 4.3.2) from thin and thick material. Finally we will obtain the radiative flux, \mathbf{F} , and mean intensity, \bar{J} , in section 4.4 below.

To simplify, we focus on one ray and drop the labeling of individual pixels, h , throughout this section.

If optically thick material of a node is detected to be spread across 2 adjacent segments in radial direction, then those segments are merged to one segment instead. To account for errors introduced by the inverse square law, we multiply by the factor $T(i,j) = R_i^2/R_j^2$ before adding the inverse square law sensitive content of segment j into segment i . These quantities are \hat{L}_{thin} , \hat{A}_{thin} and \hat{Q}_{thin} . All other quantities are not affected by the inverse square law and can

simply be added together during merging. This step is required, since we assume the optically thick material to take the shape of a compact object.

4.3.1 Optical Depth and Extinction

We assume that the optically thin matter is evenly mixed within one segment and spread over the whole volume of that segment. Together with the angular size of a ray, $\omega = 4\pi/N_{\text{pix}}$, we can compute the optical depth of a ray segment i accounting for optically thin matter, $\tau_{\text{thin},i}$, with the following equation:

$$\tau_{\text{thin},i} = \begin{cases} 0, & \text{for } i = 0 \\ \frac{\hat{A}_{\text{thin},i}}{\omega R_i^2}, & \text{for } i > 0 \end{cases} \quad (35)$$

Concerning the optically thick matter, we assume that the volume forms a compact sphere. Assuming a perfect mixing for optically thick material is overestimating the luminosity output at greater distances drastically.³ To be self-consistent with respect to previous assumptions, we compute the optical depth of the optically thick material, $\tau_{\text{thick},i}$, of segment i by

$$\omega_{\text{thick},i} = \min\left(\frac{\hat{Q}_{\text{thick},i} (\hat{V}_{\text{thick},i})^{2/3}}{\hat{V}_{\text{thick},i} R_i^2}, \omega\right), \quad (36)$$

$$\tau_{\text{thick},i} = \begin{cases} 0, & \text{for } i = 0 \\ \frac{\hat{A}_{\text{thick},i}}{\omega_{\text{thick},i} R_i^2}, & \text{for } i > 0 \end{cases} \quad (37)$$

Eq. 36 computes the angular size, $\omega_{\text{thick},i}$, of our compact volume limited to be less or equal to the angular size of a ray, ω .

The ray is integrated starting from inside going outwards. For the optically thin material we compute the extinction in the following way

$$\tau_{\text{thin},0 \rightarrow i} = \sum_{j=0}^{i-1} \tau_{\text{thin},j}, \quad (38)$$

$$\epsilon_{\text{thin},0 \rightarrow i} = \exp(-\tau_{\text{thin},0 \rightarrow i}). \quad (39)$$

Concerning the extinction caused by the optically thick material we take into account its angular size. First we compute the fraction of a ray occupied by optically thick matter, $f_{\text{thick},i}$, and its complement, $\bar{f}_{\text{thick},i}$. Secondly we compute the cumulative effects of extinction of all segments between the target and segment i , $\epsilon_{\text{thick},0 \rightarrow i}$.

$$f_{\text{thick},i} = \frac{\omega_{\text{thick},i}}{\omega}, \quad (40)$$

$$\bar{f}_{\text{thick},i} = 1 - f_{\text{thick},i}, \quad (41)$$

$$\epsilon_{\text{thick},0 \rightarrow i} = \prod_{j=0}^{i-1} (\bar{f}_{\text{thick},j} + f_{\text{thick},j} \exp(-\tau_{\text{thick},j})) \quad (42)$$

The combined extinction of optically thin and thick material working together is then straight forward computed by

$$\epsilon_{0 \rightarrow i} = \epsilon_{\text{thin},0 \rightarrow i} \cdot \epsilon_{\text{thick},0 \rightarrow i}. \quad (43)$$

³ Changing the shape of an optically thick body also changes its luminosity, as $L \propto A$ if a body is optically thick.

4.3.2 Emission

In this section we explain how we compute the flux at our target position arising from optically thin and thick material within each segment i . The equations stating the received flux (eq. 44, eq. 45 and finally eq. 46) already account for the self extinction within segment i .

The flux received from optically thin material without extinction from inner material is given by

$$F_{\text{thin},i}^* = \frac{1 - \exp(-\tau_{\text{thin},i})}{\tau_{\text{thin},i}} \times \frac{\hat{L}_{\text{thin},i}}{4\pi R_i^2}. \quad (44)$$

Eq. 44 takes into account self extinction of the material inside segment i . We direct the reader to section B for discussion of the limits of eq. 44.

The flux received from optically thick material without extinction from inner material is given by

$$F_{\text{thick},i}^* = \omega_{\text{thick},i} \frac{\hat{L}_{\text{thick},i}}{\hat{V}_{\text{thick},i}}. \quad (45)$$

Finally we compute a linear combination of both source types based on the optical depth:

$$F_i^* = \frac{F_{\text{thin},i}^* \cdot \hat{A}_{\text{thin},i} + F_{\text{thick},i}^* \cdot f_{\text{thick},i} \hat{A}_{\text{thick},i}}{\hat{A}_{\text{thin},i} + f_{\text{thick},i} \hat{A}_{\text{thick},i}}. \quad (46)$$

In order to account for the extinction of the inner part, we use $\epsilon_{0 \rightarrow i}$ from eq. 43 to compute

$$F_i = \epsilon_{0 \rightarrow i} F_i^*. \quad (47)$$

and finally sum up over all evaluation points by taking the sum

$$F = \sum_i F_i. \quad (48)$$

F is now the final flux we receive from our pixel.

4.4 Ray finalization

After section 4.3 we know the flux received from each pixel, F^h (eq. 48). To compute the net flux, \mathbf{F} , at our target position we sum up all pixels taking into account the orientation of each ray, $\hat{\mathbf{n}}^h$. Note that $\|\hat{\mathbf{n}}^h\| = 1$. Since the radiation is antiparallel with the ray, we have to introduce a minus sign. Finally we compute

$$\mathbf{F} = \sum_{h=1}^{N_{\text{pix}}} -F^h \hat{\mathbf{n}}^h. \quad (49)$$

Similar, the mean intensity, \bar{J} , can be computed by summation over all pixels and by including the local heating intensity generated by a source, J_{src} . We summarize

$$J_{\text{src}, \text{IR}} = (1 - e^{-\tau_{\text{b-node}}/2}) \frac{L_{\text{src}, \text{IR}} V_{\text{b-node}}}{V_{\text{b-node}}^{2/3} V_{\text{src}}}, \quad (50)$$

$$\bar{J} = \frac{1}{4\pi} \sum_{h=0}^{N_{\text{pix}}} F^h + J_{\text{src}, \text{IR}}, \quad (51)$$

where $\tau_{\text{b-node}} = \rho \kappa dx$ and $V_{\text{b-node}}$ are the optical depth and volume of the bottom node containing the point source, respectively. Note that $J_{\text{src}} = 0$ if the bot-node does not contain a cell. We use \bar{J} in order to heat the dust with radiation coming from surrounding material and point sources as explained in section 4.6. \bar{J} is then stored in the field `IRXE` in units $\text{erg s}^{-1} \text{cm}^{-2} \text{sr}^{-1}$.

4.5 Momentum from Flux

The momentum equation reads

$$\frac{\partial \rho \mathbf{v}}{\partial t} + \nabla (\rho \mathbf{v} \otimes \mathbf{v} + (P + P_{\text{src}})) = \frac{\kappa \rho}{c} \mathbf{F}, \quad (52)$$

where we obtain the trapped radiation pressure, P_{src} , and the flux, \mathbf{F} , as discussed in section 4.4. ρ , \mathbf{v} , P , κ and c are the density, velocity, thermal pressure and speed of light, respectively. P_{src} is the radiation pressure that is generated by the absorption of radiation within the hosting bottom node of the point source. P_{src} is computed in the following way

$$P_{\text{src}} = (1 - e^{-\tau_{\text{b-node}}/2}) \frac{L_{\text{src}}}{c A_{\text{src}}}, \quad (53)$$

where L_{src} and A_{src} are the luminosity and the area of the volume containing the source.

In the following we will explain how we compute the rate of momentum, $\dot{\mathbf{P}}$, absorbed by a cell of volume, dV , from an incoming flux, \mathbf{F} . We assume the cell to be cubic with an edge length dx . Density ρ and opacity of the cell are given by ρ and κ , respectively.

If the cell's optical depth, $\tau = \rho \kappa dx$, is low so that we can neglect extinction within the cell, we can assume the flux through the cell to be constant. In that particular case $\dot{\mathbf{P}}$ can be computed as follows

$$\dot{\mathbf{P}}_{\tau < 1} = \frac{\mathbf{F}}{c} \kappa \rho dV. \quad (54)$$

In the limit where the cell is optically thick, $\dot{\mathbf{P}}$ has to be less equal to

$$\dot{\mathbf{P}}_{\tau > 1} = \frac{\mathbf{F}}{c} dA, \quad (55)$$

where $dA = (dx)^2$ is the geometric surface of the cell.

One can compute $\dot{\mathbf{P}}$ in a scenario where \mathbf{F} is not affected by the inverse square law and hits the cube face on. In this case we find $\dot{\mathbf{P}}$ can be expressed in the following way

$$\dot{\mathbf{P}} = \frac{\mathbf{F}}{c} \kappa \rho \frac{1 - e^{-\tau}}{\tau} dV. \quad (56)$$

Note that eq. 56 recovers both limits mentioned by eq. 54 and eq. 55. Finally we store the acceleration, $\mathbf{a}_{\text{RP}} = \dot{\mathbf{P}}/\rho$, in x , y , and z direction in the fields `RPAX`, `RPAY` and `RPZ`.

The deposition of momentum by ionizing radiation onto dust is treated in an analogous manner. We receive a flux of ionizing radiation at our target position provided by `TREERAY/ONTHESPOT` (Wünsch et al. 2021) and assume a constant kappa, $\sigma_{\text{d}} = 1.5 \times 10^{-21} \text{ cm}^2$ per hydrogen atom, for UV photons. We explain the exact details of how gas and dust receive their momenta from ionized radiation in §C.

4.6 Heating and Cooling of Dust Grains

For each cell we compute the equilibrium temperature of dust by taking into account heating and cooling rates of dimension $[\text{erg cm}^{-3} \text{ s}^{-1}]$ for multiple physical processes. These processes are:

- $\Gamma_{\text{dust-gas}}$: dust grain and gas collisional interactions (Hollenbach & McKee 1979, given by eq. 3.25 of theirs),
- Γ_{ISRF} : heating by an interstellar radiation field (Bakes & Tielens 1994, given by eq. 42 of theirs) which we set to 0 here,

- Γ_{H_2} : heating from H_2 formation on grain surface (Hollenbach & McKee 1979; Glover & Mac Low 2007, their eq. 45),

- $\Lambda_{\text{BB-cool}}$: cooling by thermal emission,
- $\Gamma_{\text{BB-heat}}$: heating by thermal radiation.

We list the equations for $\Gamma_{\text{dust-gas}}$, Γ_{ISRF} and Γ_{H_2} in appendix D. During the dust temperature calculation we do not allow dust to cool beyond $T_{\text{dust, floor}} = 2.7 \text{ K}$.

The rates of the thermal radiative processes are modelled in the following way:

$$\Lambda_{\text{BB-cool}} = \rho \xi 4 \sigma \kappa T_{\text{dust}}^4, \quad (57)$$

$$\Gamma_{\text{BB-heat}} = \rho \xi 4 \pi \kappa \bar{J}, \quad (58)$$

where ρ and ξ are the density and dust to gas ratio respectively. Eq. 57 and eq. 58 together model cooling and heating due to thermal radiation accurately. In the limit, where we consider dust being embedded inside an optically thick medium, the mean intensity, J , will resemble the mean temperature of the surroundings. This is the temperature the dust will attempt to converge to. However, if the medium is optically thin along one or more `HEALPIX` generated surfaces, \bar{J} will have contributions of 0 K allowing the dust to cool and thus remove energy from the computational domain.

In combination with the effects of $\Gamma_{\text{dust-gas}}$, dust may drain energy from the gas and radiate it away given the right circumstances. These circumstances are given if the gas is substantially hotter than the dust temperature according to the mean radiative intensity, \bar{J} . We can assign a temperature to the radiation field by solving for the equilibrium between $\Lambda_{\text{BB-cool}}$ and $\Gamma_{\text{BB-heat}}$, which yields

$$T_{\bar{J}} = \sqrt[4]{\frac{\pi \bar{J}}{\sigma}}. \quad (59)$$

5 BENCHMARK OF TREERAY/RADPRESSURE

We will present results of `TREERAY/RADPRESSURE` and verify them against analytically known solutions. The tests performed within this scope include a single radiating point source (see §5.1), an optically thick blob of dust radiating thermal emission (see §5.2), dust chemistry (see §5.3) and a radiation pressure driven expansion of a bubble to verify the correct momentum deposition (see §5.4).

5.1 Point source inside a homogeneous medium

We consider a point source with a luminosity of $5.7 \times 10^4 L_{\odot}$ inside a $(0.1 \text{ pc})^3$ computational domain of homogeneous density $\rho_0 = 10^{-18} \text{ g cm}^{-3}$. We disable re-emission from dust and only consider radiation from the principal source so that we can validate the radiative transfer for a single point source in a simplified way. We perform three runs with a constant dust opacity of $\kappa_{0,\text{ext}} = 1 \text{ cm}^2 \text{ g}^{-1}$, $\kappa_{0,\text{ext}} = 10 \text{ cm}^2 \text{ g}^{-1}$ and $\kappa_{0,\text{no ext}} = 0 \text{ cm}^2 \text{ g}^{-1}$. The two groups of runs are labeled with and without extinction, respectively.

We expect the radial profile of the radiation field to

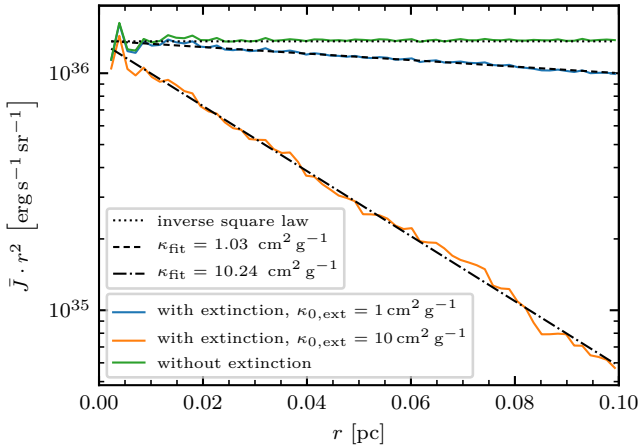


Figure 3. A single point source inside a homogeneous density medium. We compare three scenarios, two with extinction where $\kappa_{0,\text{ext}} = 1 \text{ cm}^2 \text{ g}^{-1}$ (solid blue line) and $\kappa_{0,\text{ext}} = 10 \text{ cm}^2 \text{ g}^{-1}$ (solid orange line) and one without extinction (solid green line). We show the mean intensity times the distance squared as a function of distance. Without extinction the inverse-square law is recovered. For the runs with extinction we fit an exponential to the simulation results

. We recover a dust opacity of $\kappa_{\text{fit}} = 1.03 \text{ cm}^2 \text{ g}^{-1}$ and $\kappa_{\text{fit}} = 10.24 \text{ cm}^2 \text{ g}^{-1}$ as shown by the dashed and dash-dotted lines.

follow a combination of the inverse square law and the Beer-Lambert law, namely

$$\bar{J} = \bar{J}_0 \times \frac{e^{-\tau}}{4\pi r^{-2}}. \quad (60)$$

Fig. 3 shows the mean radiative intensity times the distance squared, $\bar{J} \cdot r^2$, effectively disposing the effects of the inverse square law. Here, we expect the inverse square law to be a horizontal line as shown by the black dotted line. Our run without extinction is in agreement with the inverse square law, while the runs with extinction decreases exponentially according to the Beer-Lambert law. By fitting an exponential to the runs with extinction we recover the dust opacities with a value of $\kappa_{\text{fit}} = 1.03 \text{ cm}^2 \text{ g}^{-1}$ and $\kappa_{\text{fit}} = 10.24 \text{ cm}^2 \text{ g}^{-1}$, respectively. The dashed and dash-dotted lines in Fig. 3 show the fitted curves. Note that the momentum input is given by Eq. 56 which means that an accurate radiation field will yield the correct momentum input caused by radiation pressure in this test. This is because \mathbf{F} and $4\pi\bar{J}$ can be considered to have the same magnitude, as the single point source is the only source of radiation. In our case we are overshooting the extinction by $\sim 3\%$ and thus underestimating the momentum input from our point source.

5.2 Optically thick blob of dust

In this section we want to show that the superposition of optically thin and thick contributions add up to the correct solution.

Let us consider a spherical, optically thick body with radius r_c and density $\rho_c = 10^{-17} \text{ g cm}^{-3}$ at temperature $T_c = 30 \text{ K}$. The blob is placed inside a low density ambient medium with temperature $T_a = 10 \text{ K}$ and density

$\rho_a = 10^{-19} \text{ g cm}^{-3}$ and the background radiation temperature is set to zero. The density field of a blob with radial size r_c is given by the following equation

$$\rho(\mathbf{r}) = \begin{cases} \rho_c & \text{if } r \leq r_c \\ \rho_a & \text{else} \end{cases}, \quad (61)$$

where r is the distance measured from the centre of the blob. Such a scenario is difficult to handle for backwards ray tracing, as the geometric size of an optically thick object has to be tracked accurately, because the luminosity scales with area.

We realise 3 different blob sizes each inside a $(15 \text{ pc})^3$ sized computational domain and label them S, M and L in an increasing order. The blobs S, M and L are of size 0.75 pc, 1.5 pc and 3 pc in diameter, respectively. For each blob size we perform a run taking into account emission and absorption from the surrounding ambient medium.

Fig. 4 shows \bar{J} in a slice through $z = 0$ for S, M and L. The blobs are 2, 4 and 8 grid cells wide. The radiation field produced by the blob of hot dust are spherically symmetric in all three cases.

We perform two additional runs for S, which we label S^- and S^+ . S^- is run without emission and absorption from the ambient medium, so that \bar{J} as a function of distance approximately follows an r^{-2} profile, because the blob can be approximated by a point source at large distance. The run S^+ has an increased density of the ambient medium by a factor of 10. This causes the ambient medium to be optically thick on the length scale of the computational domain. We expect $\bar{J}(r)$ to converge to a value of 10 K, which is the equilibrium temperature, of greater distances. For the other runs, S, M and L, we expect the profile to drop below the $\bar{J}(T = 10 \text{ K})$ value, because the outer regions cool radiatively since we set the background temperature to zero.

Fig. 5 shows the mean radiation intensity, \bar{J} , as a function of distance for our five runs. The black dotted line shows the analytic solution for a point particle with a luminosity corresponding to the central dense object in the run labelled S. The analytic expression we use to model the small blob of radius R_S is given by

$$\bar{J}_S(r) = \frac{1}{4\pi} \sigma T^4 \frac{R_S^2}{r^2}. \quad (62)$$

Additionally, black horizontal lines mark the values $\bar{J}(T = 10 \text{ K})$ and $\bar{J}(T = 30 \text{ K})$. We can see that the runs S, S^+ and S^- agree with the r^{-2} profile of the black dotted line for small distances. Note that S does not reach the full 30 K value of \bar{J} because the core is only realised by $2 \times 2 \times 2$ cubic cells. Evaluating the radiation field at one of those 8 cells will create HEALPix pixel which are not populated with 30 K material so that we do not reach the full $\bar{J}(T = 30 \text{ K})$ value. For greater distances only S^- follows the r^{-2} profile, while the ambient medium contributes additional radiation in the case of S and S^+ causing deviation. S^+ does enter the expected plateau phase in the ambient medium, similar to M and L which plateau in the optically dense core at $\bar{J}(T = 30 \text{ K})$. However outside we do not see a flattening caused by the ambient medium for M and L.

From this test we conclude that the method of splitting material in optically thin and thick contributions (see section 4) converges to the correct \bar{J} in an optically thick embedded case. Also note that the interior of the core remains

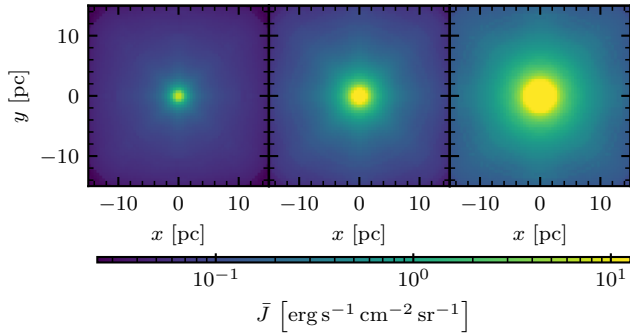


Figure 4. Slice through $z = 0$ of small (S), medium (M) and large (L) sized blobs with central temperature 30 K showing the mean radiation intensity, \bar{J} . The blobs are 2, 4 and 8 grid cells in diameter.

at constant temperature, hence there will be no acceleration caused by radiation pressure, because $\mathbf{F} = 0$ is the case in the inside. Outside in close proximity there is a region where we can model the blob to be a point source, such that $\mathbf{F} \propto r^{-2}\mathbf{e}_r$ is roughly satisfied. Further outwards, we reach a state where the ambient medium shields the radiation from the blob and dominates in emission. Again we find $\mathbf{F} = 0$ in that region.

5.3 Dust Chemistry

We show results from our method discussed in section 4.6 in this section. We setup a homogeneous density field of density $\rho_0 = 10^{-16} \text{ g cm}^{-3}$ at a gas temperature of $T_{\text{gas}} = 2000 \text{ K}$. The background radiation field is set to $T_{\text{BG}} = 0 \text{ K}$.

Dust tends to cool to the background temperature, $T_{\text{BG}} = 0 \text{ K}$, and is floored at 2.7 K . We use a dust to gas ratio of $\frac{1}{100}$. Heating of dust originates from dust-gas coupling given by $\Gamma_{\text{dust-gas}}$ within this setup. In addition, emission of dust from elsewhere may contribute to the local \bar{J} (see eq. 58) and partially stall the cooling process of dust.

Fig. 6 shows the temperature of dust and gas as a function of time for different densities, $f \times \rho_0$, where $f = 10^0, 10^{-2}, 10^{-4}, 10^{-5}, 10^{-7}, 10^{-10}$. At low densities dust and gas remain uncoupled and the dust quickly cools down to T_{min} while the gas remains warm. As the density increases, dust begins to have an impact on the gas temperature through the collisional interaction terms and vice versa. Gas and dust are heated by additional H_2 formation as the gas starts cooling down. As a function of density, the H_2 formation process happens on different timescales. Dust and gas remain at a temperature greater than 10 K as long as this process is ongoing in our test (see red, green and orange lines in fig. 6). Once this process has finished, the mixture of gas and dust is able to cool below 10 K (see orange line in fig. 6). In our test the H_2 formation is still ongoing for densities smaller than $\rho_0 \times 10^{-4}$ at the end of the simulation time resulting in temperatures between 19 K and 16 K . At densities greater than $\rho_0 \times 10^{-4}$ the formation of H_2 is completed before the simulation ends and thus the temperature is able to drop below 10 K . We show the H_2 fraction in E.

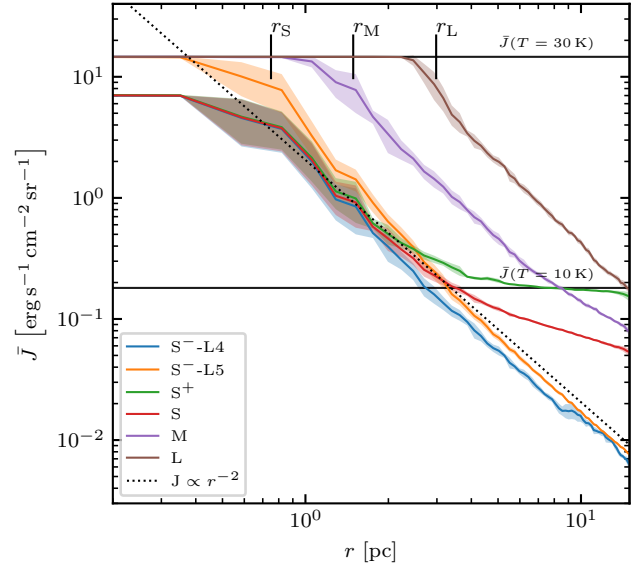


Figure 5. Radial average of the the mean intensity, \bar{J} , for different optically thick blobs of hot dust at $T_{\text{dust}} = 30 \text{ K}$ inside a 10 K cold optically thin medium. Small (S, red solid line), medium (M, purple solid line) and large (L, brown solid line) sized blobs with have a density of $\rho_c = 10^{-17} \text{ g cm}^{-3}$. Three additional runs for the small blobs are shown, one where the background medium is turned optically thick (S^+ , green solid line) and two where it is removed (S^-L4 , blue solid line, and S^-L5 , orange solid line). The run S^-L4 is run at $(64)^3$ resolution and the run S^-L5 at $(128)^3$. The shadows of the respective curves indicate the 1σ region. The black dotted line shows the Inverse-square law for an object of luminosity equal to that of model S. The black solid horizontal lines show the value of \bar{J} corresponding to 30 K and 10 K , respectively. The vertical marks labeled r_S , r_M and r_L mark the radius of the blobs S, M and L, respectively.

5.4 Radiation pressure driven bubble

In this section we want to verify that the momentum injected through radiation pressure is correct. We consider a single point source of luminosity, $L = 1/8 \times 10^6 L_{\odot}$, embedded inside a small compact spherical core of radius, $r_{\text{core}} = 0.15 \text{ pc}$, at density $\rho_c = 1.08 \times 10^{-16} \text{ g cm}^{-3}$. The mass of the core is given as $M_c = \frac{4}{3}\pi r_c^3 \rho_c$. The ambient density is $1.08 \times 10^{-28} \text{ g cm}^{-3}$. The entire setup is placed inside a $(3.0 \text{ pc})^3$ sized computational domain so that the centre of the cloud, as well as the source are positioned in one of the corners. We set the faces adjacent to the source to be reflecting (see Wünsch et al. 2021) for details on the boundary condition). By doing so we only have to simulate $1/8$ of the entire setup due to symmetry. The entire mass of the cloud is $M = 2.2 \times 10^5 M_{\odot}$, where we also take into account the mass that is not actually simulated.

The source is expected to inject radial momentum per unit time at a rate of $\dot{p} = L/c$ given that all of its radiation is absorbed. If the line of sight from the source outwards is optically thin, we expect the rate to decrease by a factor $f(r) = 1 - e^{-\tau(r)}$, where $\tau(r)$ measures the optical depth along the line of sight from the source through a thin shell at distance r . The optical depth can be calculated as the product of the surface density, $\Sigma(r) = M/4\pi r^2$, and the dust opacity, $\kappa(T)$. We compute $\Sigma(r)$ by assuming that the cloud

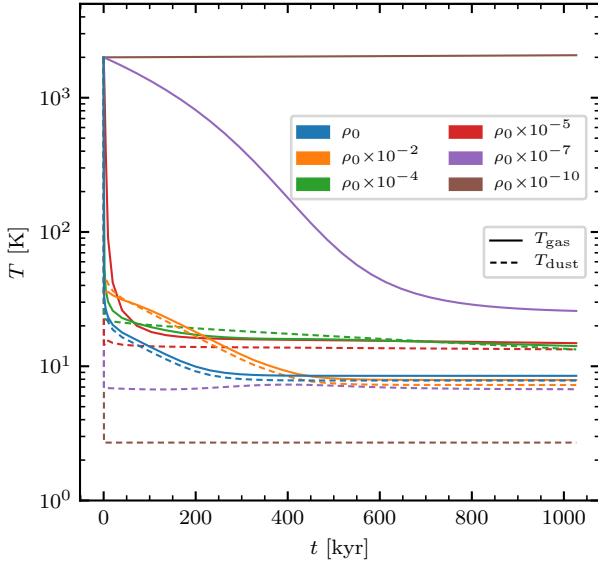


Figure 6. Dust temperature calculation showing the effects of dust cooling on the gas temperature. The initial gas temperature is set to 2000 K with $\rho_0 = 10^{-16} \text{ g cm}^{-3}$. The dust temperature is calculated according to §4.6. Dust tends to cool to $T_{\text{dust, floor}} = 2.7 \text{ K}$ radiatively but the gas dust coupling heats the dust, preventing the dust from reaching $T_{\text{dust, floor}}$. Because $\Gamma_{\text{dust-gas}} \propto \rho^2 (T_{\text{gas}} - T_{\text{dust}})$ is the case, dust gas coupling is effective at high densities and high temperature differences. Thus in the early stage dust is able to impact the gas temperature more effectively due to larger differences in temperature. In the run $\rho_0 \times 10^{-10}$ the radiative cooling of dust is stronger than the gas-dust coupling and so that dust reaches $T_{\text{dust, floor}}$.

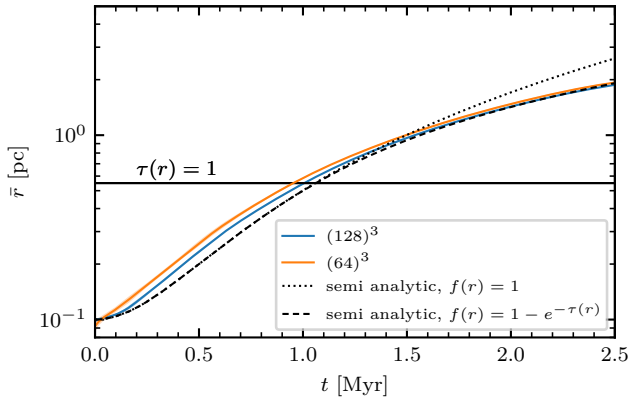


Figure 7. Radius vs time of a single source driving a bubble with radiation pressure. The blue and orange solid lines show the numerical solutions obtained through TREERAY/RADPRESSURE running with $(128)^3$ and $(64)^3$ cells, respectively. The black dotted and dashed lines show semi-analytic solutions of eq. 63 with $f(r) = 1$ and $f(r) = 1 - e^{-\tau(r)}$, respectively. The former does not account for loss of radiation through the shell becoming optically thin while expanding, while the latter does. The horizontal black solid line marks the distance at which the optical depth along the line of sight is $\tau = 1$. Above this line radiation may leak through the shell and the two semi-analytical models start to deviate.

behaves like a thin shell, where all its mass is concentrated at a radial distance, \bar{r} , and distributed smoothly across the entire angular space. The temperature, T , for $\kappa(T)$ is computed by solving for the equilibrium between the two rates given by eq. 57 and eq. 58. The equation of motion reads

$$\ddot{r} = f(r) \cdot \frac{L}{cM}, \quad (63)$$

where M denotes the mass present in the computational domain. We compute \bar{r} as:

$$M = \int dV \rho, \quad (64)$$

$$\bar{r} = \frac{1}{M} \int dV r \rho. \quad (65)$$

Fig. 7 shows the centre of mass in radial direction, \bar{r} , as a function of time for our numerical solution obtained by TREERAY/RADPRESSURE. We have performed 2 runs, a run with $(64)^3$ cells (orange solid line) and a run with $(128)^3$ cells (blue solid line). Additionally 2 other lines are shown, which are numerically integrated solutions of eq. 63, where $f(r) = 1$ (black dotted line) and $f(r) = 1 - e^{-\tau(r)}$ (black dashed line). The two semi-analytic solutions deviate past the point, where $\tau(r) < 1$ (above black solid line). As we expected the latter fits well with the results from our simulation. This is because the solution takes into account leaking of radiation. With that, the radial momentum carried by the light may also escape, as very little is absorbed, since $\tau(r)$ tends towards 0 for large values of r .

6 EXPANDING HII REGION

This section features a D-type expansion of an HII region that is radiation pressure assisted. We compare the importance of the thermal driving caused by ionisation to the radiation pressure driving for two cases. In one instance, radiation pressure will play a minuscule role for the dynamics of the HII region and in the other instance, radiation pressure will play the dominating part. Either case will be run with radiation pressure turned off and on, respectively, to highlight a direct comparison. We use similar setups to those of Rosdahl & Teyssier (2015) in their §3.

For the setup, we initiate a single source inside a computational domain of homogeneous number density, n . The source radiates at a luminosity of L corresponding to a rate of $\dot{N}_{\text{LyC}} = L/E_{\text{LyC}}$ photons in the Lyman continuum, where $E_{\text{LyC}} = 13.6 \text{ eV}$. We place the ionizing source in one corner of the computational domain and set the boundary conditions of the cube to be reflecting on all faces connected to said corner. Table 1 summarizes the parameters we use for our simulations. Radiation pressure from non-ionizing radiation is neglected and turned off. In addition, we reduce the density of cells within a distance of 2 grid cells of the source by a factor of 100.

The Strömgen radius (Strömgen 1939) is given by

$$R_s = \left(\frac{3\dot{N}_{\text{LyC}} m_p^2}{4\pi \alpha_B X^2 \rho_0^2} \right)^{1/3}, \quad (66)$$

where m_p , $\alpha_B = 2.5 \cdot 10^{-13} \text{ cm}^3 \text{ s}^{-1}$ and X are the mass of a proton, the case B recombination rate and the mass fraction of hydrogen in the neutral medium (Wünsch et al. 2021),

Table 1. This table organizes the parameters used in §6 across the two different setups in rows. The symbols n , L and t_f represent the number density, luminosity and normalization time, respectively. The variables r_D and r_{RP} are the radii the ionisation front will expand to based on the effects of D-type and RP driven expansion, respectively. Both setups run with RP turned on and off. The normalisation of time, t_f , is calculated as explained in eq. 72.

Case	n [cm ⁻³]	\dot{N}_{LyC} [s ⁻¹]	L [L_\odot]	r_{RP} [pc]	r_D [pc]	t_f [Myr]
D-type dominated	10^3	10^{49}	5.64×10^4	1.86	1.64×10^1	9.2
RP dominated	10^9	10^{52}	5.64×10^7	5.87×10^{-2}	1.64×10^{-2}	0.014

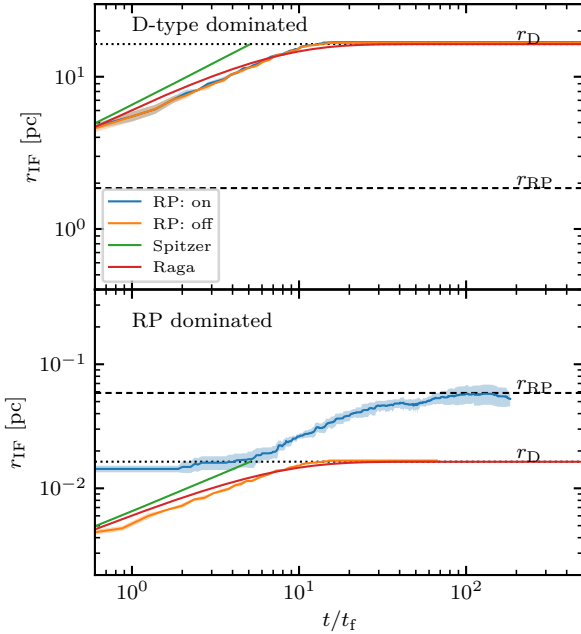


Figure 8. Radius of the ionisation front, r_{IF} , measured from the central source vs normalised time. The blue and orange lines show the runs with and without radiation pressure, respectively. The green line shows the Spitzer solution. The black dashed and dotted horizontal lines show the expected radiation pressure and ionisation driven radii r_{RP} (eq. 68) and r_D (eq. 71), respectively. The red line is the numerical solution to eq. 8 of Raga et al. (2012). The upper and lower panel show the case where D-type and RP are dominating, respectively.

respectively. The equation of motion for an ionisation front expanding into a neutral homogeneous medium is given by the Spitzer solution, namely

$$r_i = R_s \left(1 + \frac{7}{4} \frac{c_i t}{R_s} \right)^{4/7}, \quad (67)$$

where r_i measures the radius of the ionisation front and c_i the sound speed of the ionised medium.

One can express equilibrium radii at which the driving through radiation pressure and thermal expansion stalls, similar to the work of Rosdahl & Teyssier (2015). The radiation pressure is expected to be in pressure balance, if the thermal ambient medium pressure, $P_{T_0} = n_0 k T_0$, is comparable to that of the radiation pressure at the bubble surface, $P_{\text{RP}} = L/4\pi c r_{\text{RP}}^2$. In that case we find the radius to be

$$r_{\text{RP}} = \sqrt{\frac{L m_p \mu_0}{4\pi c \rho_0 k T_0}}. \quad (68)$$

A similar argument can be used to determine the final radius of the HII region driven by its D-type expansion. We expect the bubble to expand until the pressure between the ionised and neutral medium are equal, $P_i = P_0$. This relation is given by

$$n_i T_i = \frac{\rho_i}{\mu_i m_p} T_i = \frac{\rho_0}{\mu_0 m_p} T_0 = n_0 T_0, \quad (69)$$

$\rho = m_p n \mu$, μ and T are the mass density, mean molecular mass and temperature, respectively, and we label the ionised and neutral medium with the subscript i and 0 . Our source is able to keep a specified amount of hydrogen atoms ionised, according to eq. 66. Using eq. 69 and 66 for n_i yields

$$n_i = \frac{1}{X \mu_i} \sqrt{r_D^{-3} \frac{3 \dot{N}_{\text{LyC}}}{4\pi \alpha_B}}. \quad (70)$$

We can use this constraint to express n_i in terms of a corresponding radius, r_D , for the equilibrium radius of the HII region driven by heating through ionization. Finally, we arrive at

$$r_D = \left(\frac{T_i \mu_0}{T_0 \mu_i} \right)^{2/3} R_s|_{\rho_0}. \quad (71)$$

We find a slightly altered description taking into account the mean molecular weight of the neutral and ionised species in our calculations (compare their eq. 65 to our eq. 71).

We construct two cases corresponding to $r_D > r_{\text{RP}}$ and $r_{\text{RP}} < r_D$ where we turn RP on and off for each instance. We expect the presence of RP to have no effect on the run where $r_D > r_{\text{RP}}$ holds. On the other hand, we expect RP to drastically change the outcome of the runs where $r_{\text{RP}} > r_D$.

Fig. 8 shows the radial distance of the ionisation front, r_{IF} , vs. time for our different setups using TREERAY/RADPRESSURE. We determine r_{IF} as the mean distance along multiple rays aligned with the HEALPIX algorithm. The time is normalised by

$$t_f = \frac{r_D}{c_i}, \quad (72)$$

where c_i is the sound speed of the ionised medium. The top panel shows the runs where the expansion is thermal pressure dominated (i.e. $r_D > r_{\text{RP}}$). Both runs, regardless of RP being present, show almost identical dynamics of the ionisation front in the upper panel. This is because, the dominating effect is the D-type expansion itself. Their solution follows the solution of Raga et al. (2012) and converges to the limit given by r_D . The Spitzer solution is capped at r_D (dotted line) which corresponds to the D-type expansion radius from the semi-analytical solution by Raga et al. (2012) (red line). The lower panel shows the RP dominated setup. The run with RP expands more quickly and further than the run without RP. The run without RP stalls at a size in

agreement with the solution of Raga et al. (2012). The run with RP in the lower panel reaches a final radius matching r_γ given by Eq. 68 and has clearly surpassed the limits provided by r_D and the solution of Raga et al. (2012).

7 STAR FORMING SETUP

In this section, we show results from a molecular clump undergoing gravitational collapse where we form stars self-consistently. The setup is a similar setup to the one presented by Rosen et al. (2019), except for the initial turbulent velocity field.

We model the evolution of a $150 M_\odot$ massive molecular clump with an initially seeded turbulent velocity field with a power spectrum, $P(k) \propto k^{-2}$, such that the clump is sub-virial with a virial parameter of $\alpha = 0.14$. The density, ρ , follows a radial power-law profile of $\rho(r) \propto r^{-1.5}$ up to an outer cloud radius of 0.1 pc. The free fall time of the core is $t_{\text{ff}} = 42.3 \text{ kyr}$. The cloud is pressure confined by a hot low density ambient medium of temperature $T_{\text{amb}} = 2000 \text{ K}$ such that the density of the ambient medium is a factor of 100 lower than the density at the edge of the cloud. The gas temperature is set to 20 K throughout the cloud. The entire setup is housed inside a $(0.4 \text{ pc})^3$ computational domain with von Neumann boundary conditions, allowing for matter to flow in and out smoothly. We set the background infrared radiation field to $J_{\text{BG}} = 1.205 \cdot 10^{-2} \text{ erg s}^{-1} \text{ cm}^{-2} \text{ sr}^{-1}$ which corresponds to an equilibrium dust temperature of $T_{\text{BG}} = 5 \text{ K}$.

We start with a base resolution of $(128)^3$. We adaptively refine the grid to ensure that the Jeans length is refined by at least 8 grid cells following the conditions of Truelove et al. (1997) to prevent artificial fragmentation. We allow for up to 5 additional levels of refinement such that the highest resolution of this simulation is 20 AU. If the Jeans length is refined by 16 or more cells, we derefine. Condensations within our core arise self-consistently through gravitational collapse. Eventually, they may form sink particles, which can only be formed on the highest refinement level. Throughout the simulation we keep cells hosting sink particles on the highest level of refinement. We treat sink particles as described in §3.1.

7.1 Morphology across time

The initial spherically symmetric configuration is quickly disturbed by the turbulent velocity field. Local high density regions are forming where streams of momentum, $\rho \mathbf{v}$, collide. In those regions the gas is heated through $p dV$ work (adiabatic compression). The dust is heated by the gas through collisional interactions, whilst trying to cool by radiating in the continuum infrared. As a result, the dust temperature is settling in between the gas temperature, T_{gas} , and the radiation temperature, T_j (see eq. 59), as described in §4.6. Fig. F2 shows the density, ρ , gas and dust temperatures, and the radiation temperature, T_j , across different times for the entire computational domain. We can see that T_j is hottest at the central hub and decreases further out. This indicates that the central hub is dominating the IR luminosity output. As the simulation evolves, the radiation temperature

increases globally, which can be seen most significantly comparing the times $0.4 t_{\text{ff}}$ and $0.5 t_{\text{ff}}$. The increased radiation temperature also heats the dust and therefore indirectly the gas at greater distances further out.

7.2 Stellar population

Fig. 9 shows an overview over the stellar population, showing the mass, accretion rate, luminosity and number of ionising photons vs. time. Early on, at around $0.1 t_{\text{ff}}$ the first stellar object, labeled '1', forms in the central dense hub. Throughout the simulation '1' stays the most massive object and with that it is the most dominant source of stellar feedback. After its formation the simulation enters a quiescent phase, where no stars are formed for about another $0.2 t_{\text{ff}}$. This is followed by a phase of frequent star formation taking place outside of the central hub in the dense filamentary material accreting onto the central hub (see Fig. 10 at $t = 0.4 t_{\text{ff}}$). These stellar objects follow the general trend of the infalling gas and migrate to the central hub (see Fig. 10 and Fig. 11). Inside the central hub their accretion rate is minuscule compared to the primary star embedded in the center. It is only a brief time during which the secondary sink particles accrete and after which their accretion drops significantly. Looking at their luminosity in the upper right panel of Fig. 9 one can see that the luminosity output of the secondary sink particles is dominated by their stellar luminosity due to the lack of accretion. Overall, the motion of the secondary sink particles is governed by the gravity of the central star and gas. The lower right panel of Fig. 9 shows the rates of photons emitted in the Lyman continuum, \dot{N}_{LYC} , both from the stellar and hot spot accretion separately. The most massive star manages to form a very compact HII region between $0.4 t_{\text{ff}}$ and $0.5 t_{\text{ff}}$ (looking at the phase diagram, Fig. 12). We show an exemplary spectral emission diagram at $t = 0.163 t_{\text{ff}}$ of the primary sink particle in Fig. F1.

7.3 The Role of Dust

7.3.1 Heating and Cooling

With TREERAY/RADPRESSURE and our chemistry network (see §4.6) we can follow the dust temperature evolution. Fig. 12 shows phase diagrams of gas, dust and radiation across different times.

We consider gas with $\rho < 10^{-19} \text{ g cm}^{-3}$ to be part of the initial background medium. Throughout time the background medium is cooling down. Gas at densities $10^{-19} \text{ g cm}^{-3} < \rho < 10^{-16} \text{ g cm}^{-3}$ behaves mostly isothermal and is able to cool down over time via dust, since the radiation temperature is lower than the dust temperature. One can see this in Fig. 12 where T_j is significantly lower than the dust temperature at $t = 0.2 t_{\text{ff}}$. Over time T_j increases and hence the ability of dust to cool efficiently fades. The forming stars become more embedded as time progresses because of gravitational collapse, which forms compact structures. The average optical depth along all lines of sight at a given position increases. This causes the radiation temperature to increase due to contributions from hotter surrounding material. At later times one finds the luminosity output of the central object to be significant enough to influence T_{dust} even at greater distances, where the densities

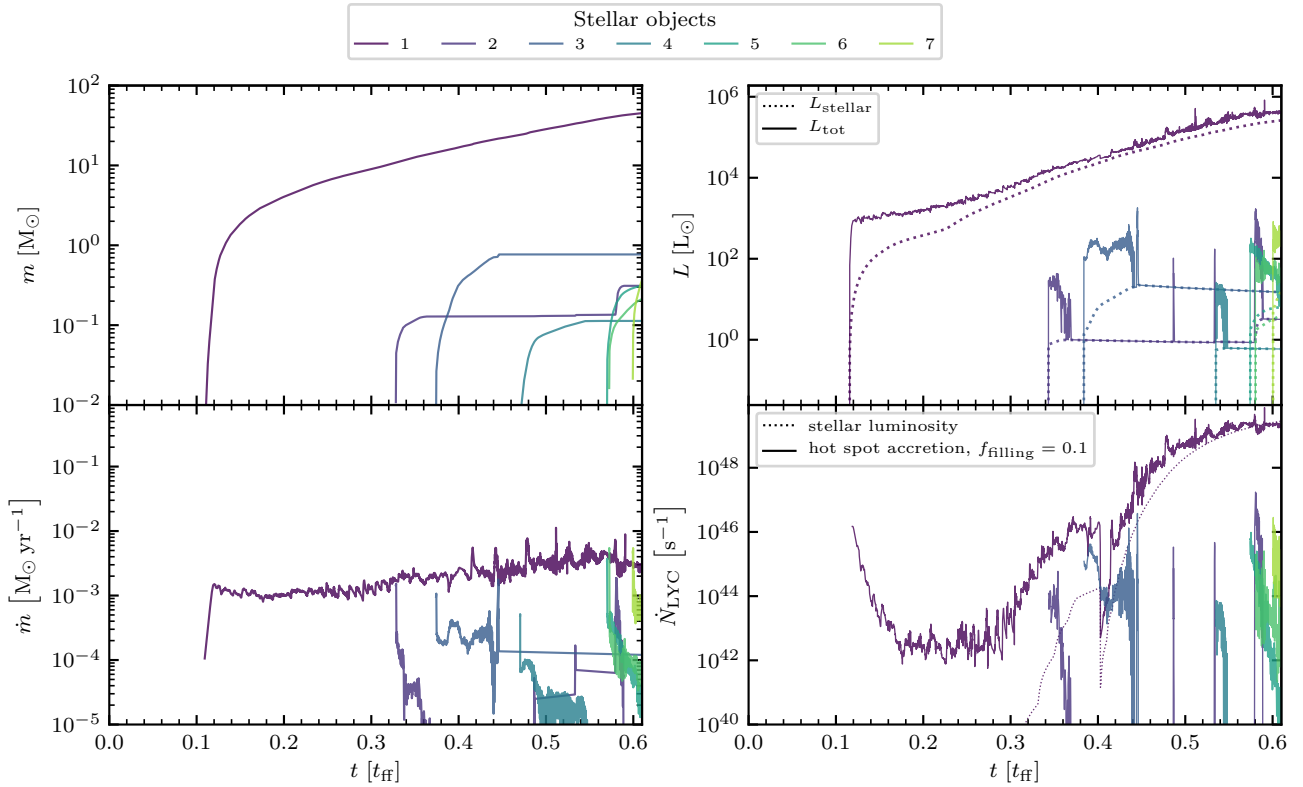


Figure 9. We show the mass, m , luminosity, L , accretion rate, \dot{m} , and rate of ionizing photons, \dot{N}_{LYC} , vs time in this plot. In total we form 6 stellar objects represented by sink particles. The most massive star, labeled 1, forms early on embedded in the center (see Fig. 11). It is the most massive star (see left upper panel) and the dominating source of radiation (see upper right panel) throughout time.

are lower. Here we find $T_{\bar{J}} \approx T_{\text{dust}} > T$. We can also see the effects of accretion shock heating in the gas temperature at intermediate densities. Initially only a subtle characteristic can be found at $t = 0.2 t_{\text{ff}}$ at around $\rho = 10^{-16} \text{ g cm}^{-3}$, where the temperature spikes for a small fraction of the gas. At later times we find the feature of accretion shock heating to be more pronounced and shifted towards lower densities. This is because gas from the outer parts of the cloud starts hitting the central hub, which is at lower density due to the power-law profile. In addition, the kinetic energy, which the gas from the outside is accreting onto the central hub is increasing, resulting in more thermal energy upon impact. This results in the growing peak of accretion shock heating. Because dust is coupled to the gas in this density regime (see Fig. 6), we find corresponding peaks in the dust and radiation temperatures at similar densities as well.

Fig. 13 shows phase diagrams for the gas and radiation temperature vs. dust temperature at different times. The magenta dotted line indicates the 1 to 1 line. We can see that most of the gas is located around the 1 to 1 line in the left column at $t = 0.2 t_{\text{ff}}$. At higher temperatures gas is located above the 1 to 1 line which allows gas to be cooled through dust, as $T > T_{\text{dust}}$. In addition, dust is hotter compared to the radiation temperature, which can be seen in the right column where the majority of the mass is well below the 1 to 1 line. With increasing time, gas and radiation move closer to the 1 to 1 line, such that radiative cooling becomes less effective. The decrease in cooling efficiency allows both

dust and gas to move upwards along the 1 to 1 line reaching higher temperatures with time. The accretion shocked gas can be seen at high gas temperatures at around 10^2 K to 10^3 K while being far from the 1 to 1 line. Typically one finds this type of gas on the boundary of dense structures, giving the gas suitable conditions to be cooled by radiation. We find dust to follow the 1 to 1 line in the center of the core. Here dust can not cool as efficiently as on the boundary thus resulting in accumulation near the 1 to 1 line. This behaviour can be seen in fig. 13 in the right column at $t \geq 0.5 t_{\text{ff}}$. Here dust is surrounded by optically thick material radiating at its own temperature making it unable to cool.

7.3.2 Radiation Pressure

We find that gravity dominates over RP in the early stages. Fig. 14 shows a projection of the density along the line of sight and density-weighted acceleration due to RP, \mathbf{a}_{RP} , gravity and RP, $\mathbf{a}_{\text{RP}} + \mathbf{a}_{\text{G}}$, and gravity, \mathbf{a}_{G} . All accelerations shown are projected in the radial direction of the most massive star, where positive values of $\mathbf{a}_{\text{RP}} \cdot \hat{\mathbf{r}}_{\text{star}}$ and $\mathbf{a}_{\text{G}} \cdot \hat{\mathbf{r}}_{\text{star}}$ point away from the star. We can see that the region only close to the star is affected by radiation pressure and turns super Eddington, $\mathbf{a}_{\text{RP}} \cdot \hat{\mathbf{r}}_{\text{star}} > -\mathbf{a}_{\text{G}} \cdot \hat{\mathbf{r}}_{\text{star}}$, at later times. But still the pressure caused gravity pulling gas towards the center overcomes the radiation pressure.

Fig. 15 shows the mass weighted probability density function (PDF) of RP and gravitational acceleration across

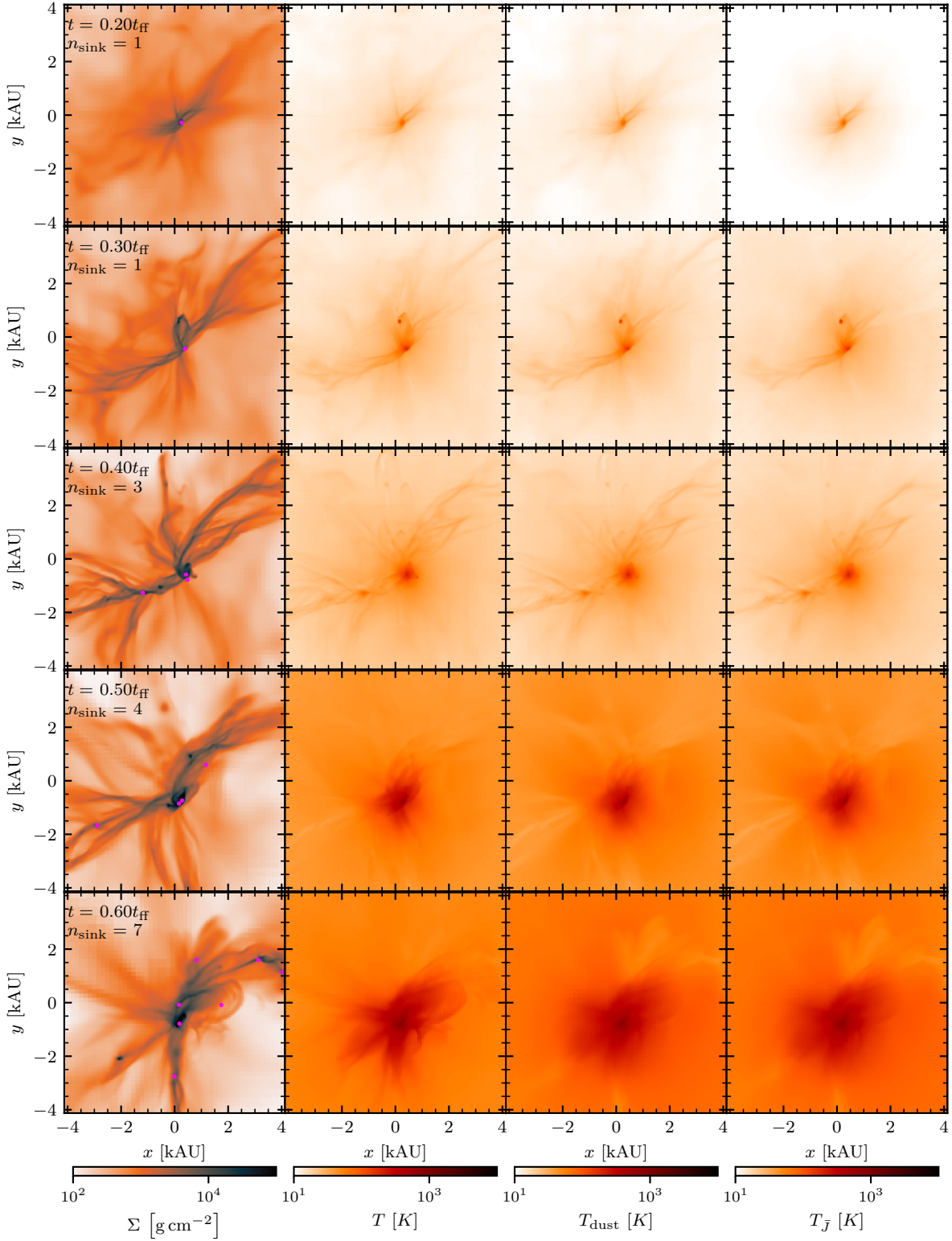


Figure 10. Projections along the z -coordinate axis of an $(8 \text{ kAU})^3$ cube around the origin for the turbulent star forming test (see §7). Organized in rows we show, from left to right, the column density and the density weighted gas temperature, dust temperature and radiation temperature across different times (top to bottom). The time, t , is measured in free-fall times, $t_{\text{ff}} = 42.3 \text{ kyr}$. The number of formed sink particles present is labeled n_{sink} . We can see stars forming in the central hub initially and later on forming in dens structures connected to the hub further out. The central hub is hotter than the ambient medium with gas and dust temperatures of around 100 K to 1000 K. At around $t = 0.5 t_{\text{ff}}$ the luminosity output of the central hub increases, heating up the surrounding material.

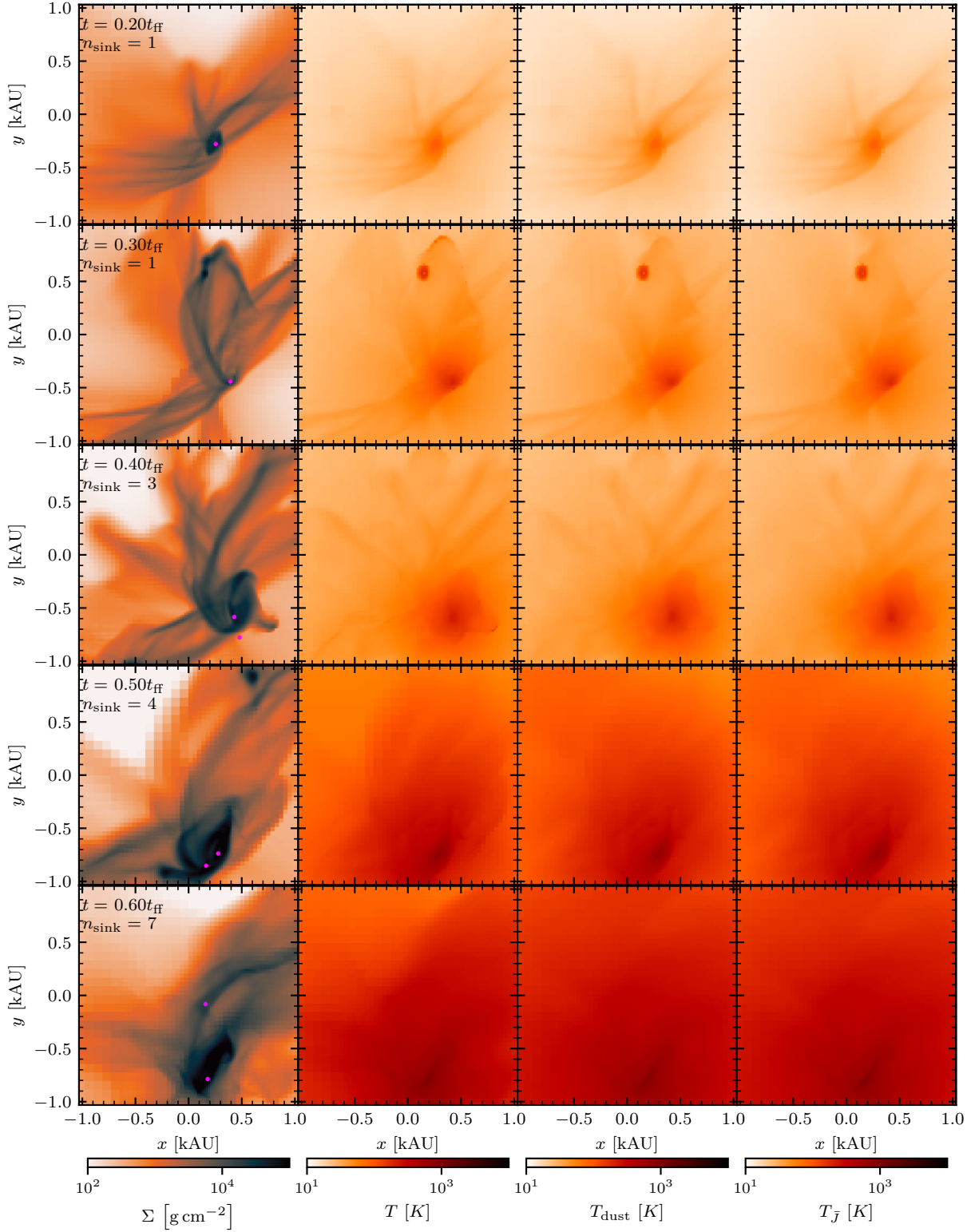


Figure 11. Same as Fig. 10 but for a $(2 \text{ kAU})^3$ cube around the origin. We can see the central hub hosting the the most massive star across time. At $t = 0.3 t_{\text{ff}}$ we can see a radiatively driven outflow towards the positive y -direction, which later on falls back on the central hub. The central hub gets collectively hotter over time concerning all three temperatures.

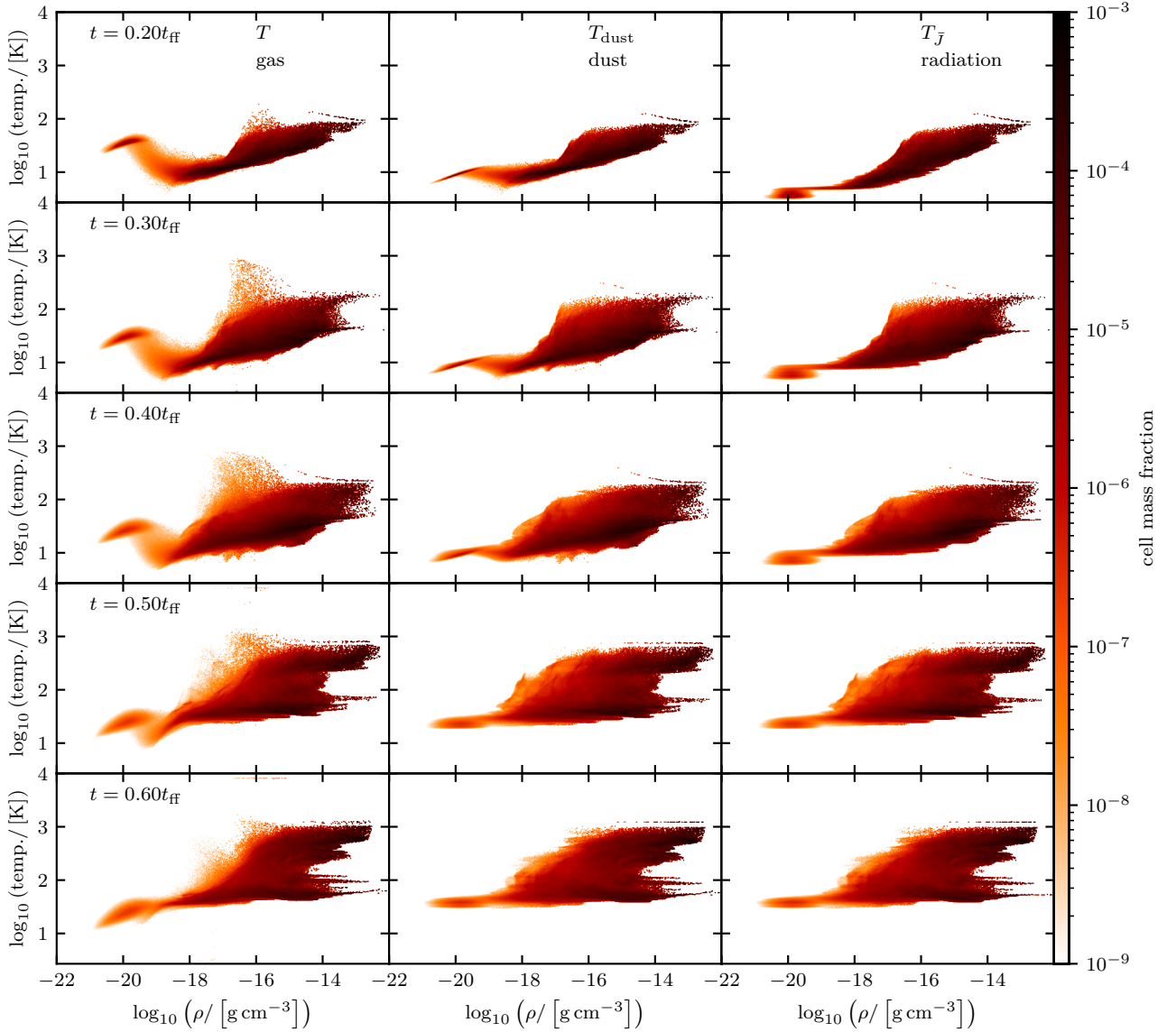


Figure 12. Phase diagrams of the gas, dust and radiation temperature (from left to right) for different times (from top to bottom). All cells are normalised by the total mass in the computational domain. The clump at $\rho \approx 10^{-20} \text{ g cm}^{-3}$ and $T \approx 10^2 \text{ K}$ resembles the background medium which is slowly cooled by the dust. The very dense part at around $\rho \approx 10^{-14} \text{ g cm}^{-3}$ and $T \approx 10^2 \text{ K}$ shows the central hub getting hotter over time. Throughout time we see the trend that, $T > T_{\text{dust}} > T_J$ is well established in the lower density regions. This enables the dust to cool the gas by radiating the thermal energy away. Eventually the global minimum radiation temperature increases and with it the gas and dust temperature follow.

different times. We find the changes in the gravitational spectrum to be minuscule compared to the changes in the RP spectrum with increasing time. The RP spectrum tends towards higher values with an increasing luminosity output of the central hub.

8 CONCLUSION

This work presents a novel method to compute the radiative transfer of the infrared radiation by dust and stars on-the-fly in three-dimensional simulations of e.g. star formation.

In particular, every cell in the computational domain and any number of present (sink) particles can be a source of radiation. The general idea of the method can be transferred to compute radiative transfer on other macroscopic sources of radiation (e.g. sources that can not be considered as point sources like stars in a numerical simulation). We find that with a computational expense of $N \log(N)$, where N is the number of grid cells (as for the original implementation in Wunsch et al. (2021)), TREERAY/RADPREESURE is applicable to solve large scale problems.

In a first step, for each grid cell,

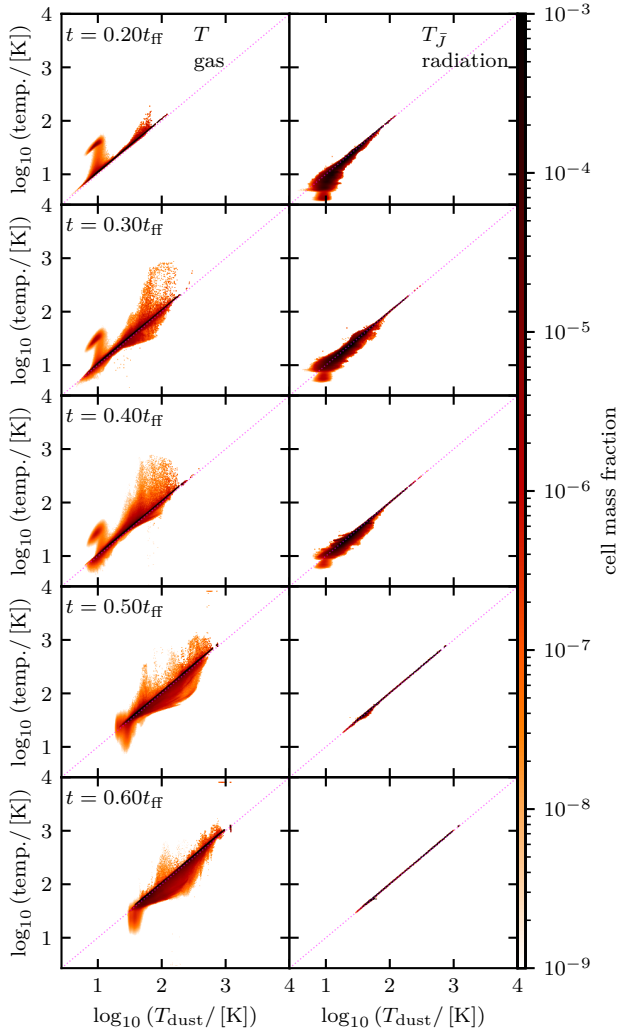


Figure 13. Phase diagrams of gas and radiation temperature vs dust temperature organized in columns. The phase diagrams are grouped into rows for different times. The dotted magenta line shows the 1 to 1 line. The cells are normalised to the current mass present in the entire computational domain. Most of gas and dust follow the 1 to 1 line with slight deviation (left column). The accretion shock heated gas is in a state able to be cooled by gas effectively ($T_{\text{dust}} < T$). Dust is mostly hotter than the local radiation temperature (right column), which allows dust to cool radiatively.

TREERAY/RADPRESSURE maps contributions from dust and point sources (e.g. stars) onto rays along different directions, where each ray has an associated angular size similar to the shape of a cone. The rays span the surface of the unit sphere according to the HEALPix algorithm (typically we use 48 rays). Subsequently, each ray is integrated to compute a radiative intensity along its line of sight. With all rays integrated, a radiative flux and mean intensity are calculated. We take into account that the Planck-mean dust opacity is temperature-dependent. Finally, we compute the radiation pressure on dust by infrared radiation and its heating rate.

The novel approach presented in this work also couples the infrared radiative transfer to a chemical network (see §4.6). In particular, the mean intensity of the infrared radiation serves as an input for the thermal equilibrium calculation of the dust temperature, i.e. the dust is heated by IR radiation. In this way, we are able to model the interplay of dust and gas in a self-consistent way. Given that a region is not deeply embedded, dust may cool gas through collisional interactions and radiate thermal energy away. In that case we recover an almost isothermal behavior. On the other hand, an embedded region behaves close to adiabatic if radiation can not escape efficiently. Our method allows to model radiative cooling in both embedded and exposed conditions.

The tests presented in §5 show that we can reproduce the Beer-Lambert law and correct radiative energy profiles in optically thin and thick regimes. We are able to compute radiative transfer from macroscopic objects such as dense blobs as presented in §5.2. We verify the correct momentum transfer caused by radiation pressure onto dust and show that the method allows for the leakage through optically thin media as shown in §5.4.

Next, we connect the TREERAY/RADPRESSURE module with the TREERAY/ONTHESPOT module (Wünsch et al. 2021), which treats the transport of ionizing radiation and the associated momentum input on gas and dust. In §6, we show that the combined method faithfully models the expansion of an HII region in two different environments. We find that RP drives the expansion of an ultra-compact HII region over its limitation given by the pressure balance of the ionised medium and its surroundings.

In addition to the tests, we simulate massive star formation in a collapsing, turbulent prestellar core. The star forming setup highlights accretion shock heated gas on the boundary of filaments and the central hub. We find that dust is picking up thermal energy through collisional coupling with gas, resulting in dust temperatures slightly below 100 K. Under those circumstances, where dust is not fully surrounded by other hot dust, dust is able to radiatively cool. On the other hand, dust is not able to cool in the dense region close to the central star, where the local radiation temperature and dust temperature are equal. For times later than $0.5 t_{\text{ff}}$ gas may be warmer than dust due to accretion shock heating and in other instances, gas may be colder than dust due to insufficient dust-gas coupling where dust is radiatively heated. We find that the dust temperature is in agreement with the radiation temperature past $0.5 t_{\text{ff}}$. At later times Radiation pressure is minuscule compared to the effects of gravity in the early stage. The luminosity output of the central hub grows with the mass of the stellar population over time and with it, the feedback through ionisation and RP. RP initially dominates the feedback and drives a cavity within which an ultra compact HII region forms. Eventually the gas may be blown away through the stellar feedback.

Our method, TREERAY/RADPRESSURE, is a first approach towards solving RT of extended sources and we plan on improving it further in future works, e.g. we plan to treat the effects of scattering on dust in future works. We aim at analysing the star forming setup in greater detail in a separate publication.

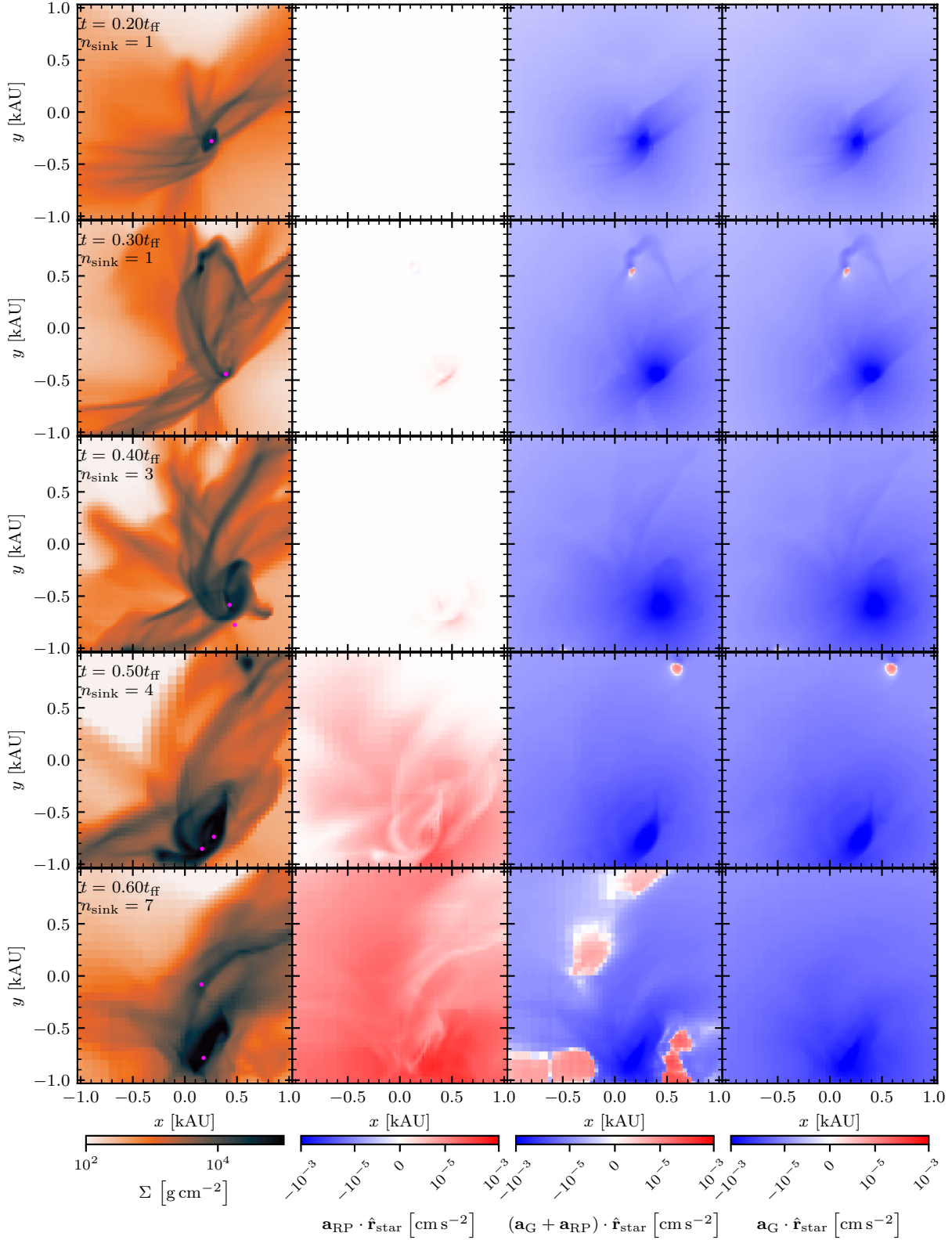


Figure 14. Similar to Fig. 11, we show projections along the z -axis of a $(2 \text{ kAU})^3$ cube around the origin. From left to right we show again the column density (for reference) and 3 different radial accelerations. All 3 acceleration vectors are density weighted along the line of sight and projected on the line of sight towards the most massive star. Going from left to right we have the RP acceleration, the acceleration due to gravity and RP combined, and the gravitational acceleration. We can see that RP manages to oppose gravity close to the central star over time.

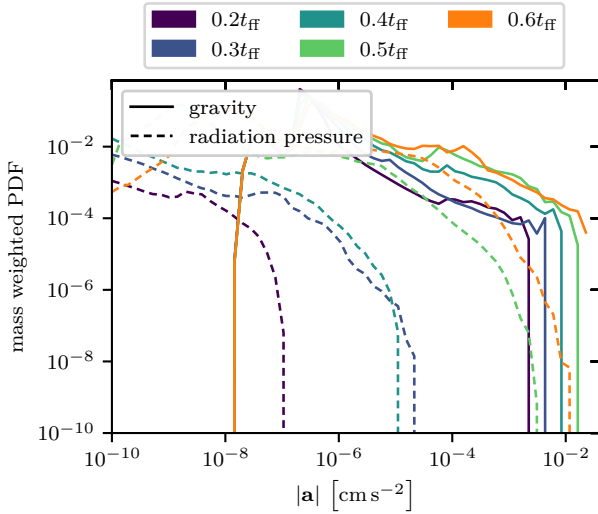


Figure 15. Mass weighted PDF of acceleration exerted as a consequence of gravity and radiation pressure across time. The impact of radiation pressure is increasing over time towards higher accelerations while the spectrum of gravity does not change by a lot.

ACKNOWLEDGEMENTS

AK, SW, and SH gratefully acknowledge the European Research Council under the European Community's Framework Programme FP8 via the ERC Starting Grant RAD-FEEDBACK (project number 679852). SW and SH further thank the Deutsche Forschungsgemeinschaft (DFG) for funding through SFB 956 "The conditions and impact of star formation" (sub-project C5). DS acknowledges the DFG for funding through SFB 956 "The conditions and impact of star formation" (sub-project C6). RW acknowledges support by project 19-15008S of the Czech Science Foundation and by the institutional project RVO:67985815. FD gratefully acknowledges funding from the Grant Agency of the Czech Republic under grant number 20-21855S. The software used in this work was in part developed by the DOE NNSA-ASC OASCR Flash Center at the University of Chicago. The authors gratefully acknowledge the Gauss Centre for Supercomputing e.V. (www.gauss-centre.eu) for funding this project by providing computing time through the John von Neumann Institute for Computing (NIC) on the GCS Supercomputer JUWELS at [Jülich Supercomputing Centre](https://www.juwi.de) (2021) (JSC). We particularly thank the Regional Computing Center Cologne for providing the computational facilities for this project by hosting our supercomputing cluster "Odin".

DATA AVAILABILITY

The data underlying this article will be shared on reasonable request to the corresponding author.

REFERENCES

Abel T., Wandelt B. D., 2002, *MNRAS*, **330**, L53

- Baczynski C., Glover S. C. O., Klessen R. S., 2015, *MNRAS*, **454**, 380
- Bakes E. L. O., Tielens A. G. G. M., 1994, *ApJ*, **427**, 822
- Bisbas T. G., et al., 2015, *MNRAS*, **453**, 1324
- Calvet N., Gullbring E., 1998, *ApJ*, **509**, 802
- Clarke S. D., Whitworth A. P., Duarte-Cabral A., Hubber D. A., 2017, *MNRAS*, **468**, 2489
- Dinnbier F., Walch S., 2020, *MNRAS*, **499**, 748
- Draine B. T., 2011, *ApJ*, **732**, 100
- Federrath C., Banerjee R., Clark P. C., Klessen R. S., 2010, *ApJ*, **713**, 269
- Fryxell B., et al., 2000, The Astrophysical Journal Supplement Series, **131**, 273
- Glover S. C. O., Mac Low M.-M., 2007, *ApJS*, **169**, 239
- Górski K. M., Hivon E., Banday A. J., Wandelt B. D., Hansen F. K., Reinecke M., Bartelmann M., 2005, *ApJ*, **622**, 759
- Grond J. J., Woods R. M., Wadsley J. W., Couchman H. M. P., 2019, *MNRAS*, **485**, 3681
- Haid S., Walch S., Seifried D., Wunsch R., Dinnbier F., Naab T., 2018, *MNRAS*, **478**, 4799
- Haid S., Walch S., Seifried D., Wunsch R., Dinnbier F., Naab T., 2019, *MNRAS*, **482**, 4062
- Hollenbach D., McKee C. F., 1979, *ApJS*, **41**, 555
- Jülich Supercomputing Centre 2021, *Journal of large-scale research facilities*, **7**
- Kannan R., Vogelsberger M., Marinacci F., McKinnon R., Pakmor R., Springel V., 2019, *MNRAS*, **485**, 117
- Kessel-Deynet O., Burkert A., 2000, *MNRAS*, **315**, 713
- Kim J.-G., Kim W.-T., Ostriker E. C., 2018, *ApJ*, **859**, 68
- Klassen M., Pudritz R. E., Peters T., 2012, *MNRAS*, **421**, 2861
- Krumholz M. R., Thompson T. A., 2012, The Astrophysical Journal, **760**, 155
- Krumholz M. R., Klein R. I., McKee C. F., Bolstad J., 2007, *ApJ*, **667**, 626
- Kuiper R., Hosokawa T., 2018, *A&A*, **616**, A101
- Kuiper R., Yorke H. W., Mignone A., 2020, arXiv e-prints, [p. arXiv:2009.12374](https://arxiv.org/abs/2009.12374)
- Lepp S., Shull J. M., 1983, *ApJ*, **270**, 578
- Levermore C. D., 1984, *J. Quant. Spectrosc. Radiative Transfer*, **31**, 149
- Levermore C., Pomraning G., 1981, The Astrophysical Journal, **248**, 321
- Martin P. G., Schwarz D. H., Mandy M. E., 1996, *ApJ*, **461**, 265
- Matzner C. D., 2002, *ApJ*, **566**, 302
- Menon S. H., Federrath C., Krumholz M. R., Kuiper R., Wibking B. D., Jung M., 2022, *MNRAS*, **512**, 401
- Mihalas D., Mihalas B. W., 2013, Foundations of radiation hydrodynamics. Courier Corporation
- Raga A. C., Cantó J., Rodríguez L. F., 2012, *MNRAS*, **419**, L39
- Rosdahl J., Teyssier R., 2015, Monthly Notices of the Royal Astronomical Society, **449**, 4380
- Rosen A. L., Krumholz M. R., Oishi J. S., Lee A. T., Klein R. I., 2017, *Journal of Computational Physics*, **330**, 924
- Rosen A. L., Li P. S., Zhang Q., Burkhardt B., 2019, *ApJ*, **887**, 108
- Semenov D., Henning T., Helling C., Ilgner M., Sedlmayr E., 2003, *Astronomy & Astrophysics*, **410**, 611
- Shapiro P. R., Kang H., 1987, *ApJ*, **318**, 32
- Spitzer L., 1978, Physical processes in the interstellar medium. New York Wiley-Interscience, 1978. 333 p.
- Strömberg B., 1939, *ApJ*, **89**, 526
- Tan J. C., Beltrán M. T., Caselli P., Fontani F., Fuente A., Krumholz M. R., McKee C. F., Stolte A., 2014, in Beuther H., Klessen R. S., Dullemond C. P., Henning T., eds, Protostars and Planets VI. p. 149 ([arXiv:1402.0919](https://arxiv.org/abs/1402.0919)), [doi:10.2458/azu_uapress_9780816531240-ch007](https://doi.org/10.2458/azu_uapress_9780816531240-ch007)
- Thompson T. A., Quataert E., Murray N., 2005, The Astrophysical Journal, **630**, 167

Truelove J. K., Klein R. I., McKee C. F., Holliman John H. I., Howell L. H., Greenough J. A., 1997, *ApJ*, **489**, L179
 Wunsch R., Walch S., Dinnbier F., Whitworth A., 2018, *MNRAS*, **475**, 3393
 Wunsch R., Walch S., Dinnbier F., Seifried D., Haid S., Klepitko A., Whitworth A. P., Palouš J., 2021, arXiv e-prints, p. arXiv:2105.09644

APPENDIX A: INFORMATION PROPAGATION UPWARDS THE TREE

In this section we explain how quantities are propagated upwards the octtree. The crucial part is to store optically thin and thick contributions separately to maintain accuracy. In our implementation we propagate b-nodes and h-nodes differently in order to save memory on the biggest layer, made up of b-nodes. If the sub-node is a bottom node, we do the following:

$$\underline{L}_{\text{h-node, thick}} = \sum_{k}^{\tau_{\text{b-node}} \geq 1} \underline{L}_{\text{b-node, thick}, k}, \quad (\text{A1})$$

$$V_{\text{h-node, thick}} = \sum_{k}^{\tau_{\text{b-node}} \geq 1} V_{\text{b-node}, k}, \quad (\text{A2})$$

$$\tilde{A}_{\text{h-node, thick}} = \sum_{k}^{\tau_{\text{b-node}} \geq 1} \tilde{A}_{\text{b-node}, k}, \quad (\text{A3})$$

$$L_{\text{h-node, thin}} = \sum_{k}^{\tau_{\text{b-node, thick}} < 1} L_{\text{b-node, thin}, k} + S_{\text{b-node}, k} \quad (\text{A4})$$

$$V_{\text{h-node, thin}} = \sum_{k}^{\tau_{\text{b-node}} < 1} V_{\text{b-node}, k}, \quad (\text{A5})$$

$$\tilde{A}_{\text{h-node, thin}} = \sum_{k}^{\tau_{\text{b-node}} < 1} \tilde{A}_{\text{b-node}, k}. \quad (\text{A6})$$

Otherwise, if the sub-nodes consist of h-nodes, we simply compute

$$X_{\text{h-node}, Y} = \sum_{k}^{\text{b-node}} X_{\text{b-node}, Y, k}, \quad (\text{A7})$$

where X may be, L , \tilde{A} , V or S and Y , thin or thick, respectively.

Since a higher level node may contain optically thin and thick contributions at the same instance, we need to store them separately. Eq. A1, eq. A2 and eq. A3 trace optically thick quantities, while eq. A4, A5, and eq. A6 trace optically thin contributions.

In addition we compute the centre of luminosity (COL), \mathbf{r}_{COL} , as seen from the geometric centre of the node, \mathbf{r}_{O} , for higher level nodes. Again we distinguish if the sub-nodes are b-nodes or h-nodes. In the former case we compute

$$\xi_{\text{b-node}} = L_{\text{b-node}}, \quad (\text{A8})$$

if the b-node is optically thin and

$$\xi_{\text{b-node}} = L_{\text{b-node}} \cdot (V_{\text{b-node}})^{2/3}, \quad (\text{A9})$$

otherwise. If the sub-nodes are h-nodes we use

$$\xi_{\text{h-node}} = L_{\text{h-node, thin}} + \underline{L}_{\text{h-node, thick}} \cdot (V_{\text{h-node, thick}})^{2/3} \quad (\text{A10})$$

Finally we compute:

$$\Xi_{\text{h-node}} = \sum_{k}^{\text{sub-nodes}} \xi_{\text{sub-node}, k}, \quad (\text{A11})$$

$$\mathbf{r}_{\text{h-node, COL}} = \frac{1}{\Xi} \sum_{k}^{\text{sub-nodes}} \xi_{\text{sub-node}, k} \mathbf{r}_{\text{sub-node}, k}, \quad (\text{A12})$$

where $\mathbf{r}_{\text{sub-node}, k}$ is the position of the sub-node relative to \mathbf{r}_{O} .

APPENDIX B: LIMITS OF AN OPTICALLY THIN AND THICK SEGMENT

Here we want to show, that eq. 44 has the correct limits if the material inside segment i becomes optically thin or thick. To do this we consider $\tau_{\text{thin}, i} \ll 1$ and $\tau_{\text{thin}, i} \gg 1$.

By using a Taylor expansion series one can show that all terms involving $\tau_{\text{thin}, i}$ collapse to unity in the former case. We arrive at

$$\text{eq. (44)} \quad \tau_{\text{thin}, i} \ll 1 \quad \approx \quad \frac{\hat{L}_{\text{thin}, i}}{4\pi R_i^2}. \quad (\text{B1})$$

Expression B1 is as expected, as would indeed see all luminosity content of segment i to be radiating. This solution is similar to that of a point source.

In the latter case all terms involving $\tau_{\text{thin}, i}$ can be approximated by $1/\tau_{\text{thin}, i}$. The complete relation can be expressed in the following way

$$\text{eq. (44)} \quad \tau_{\text{thin}, i} \gg 1 \quad \approx \quad \frac{1}{\tau_{\text{thin}, i}} \times \frac{\hat{L}_{\text{thin}, i}}{4\pi R_i^2}. \quad (\text{B2})$$

Next we can introduce a factor of unity of the form $\frac{A_i}{A_i}$, where $A_i = \omega R_i^2$ is the area of segment i measured in angular direction. Together with $1/\tau_{\text{thin}, i}$ we can express this as

$$\frac{A_i}{A_i} \times \frac{1}{\tau_{\text{thin}, i}} = \frac{A_i}{\hat{A}_{\text{thin}, i}} \quad (\text{B3})$$

by using the definition of eq. 35. Substituting eq. B3 into eq. B2 results in the following expression

$$\text{eq. (44)} \quad \tau_{\text{thin}, i} \gg 1 \quad \approx \quad \frac{\omega R_i^2}{4\pi R_i^2} \times \frac{\hat{L}_{\text{thin}, i}}{\hat{A}_{\text{thin}, i}}. \quad (\text{B4})$$

The left factor yields $1/N_{\text{pix}}$. The factor on the right hand side can be understood as optical depth weighted mean temperature by considering that each segment sums over the each node's quantities described by eq. 20 and eq. 21. Finally we arrive at

$$\text{eq. (44)} \quad \tau_{\text{thin}, i} \gg 1 \quad \approx \quad \frac{4\pi}{N_{\text{pix}}} \times \frac{\sigma}{\pi} \langle T_{\text{dust}}^4 \rangle_{\rho dV_K}. \quad (\text{B5})$$

Note that eq. B5 is in agreement with eq. 45 which describes the flux seen from optically thick material contained within a ray's segment. The difference is that the optically thin material is stretched over the entire pixel and thus shining over the full ray's solid angle $\omega = \frac{4\pi}{N_{\text{pix}}}$ while the optically thick material is not, but compact instead. This approximates the optically thick material to radiate from its surface.

APPENDIX C: RADIATION PRESSURE ON DUST AND GAS BY UV RADIATION

For a given flux of ionizing photons per unit time and area, \dot{N}_{ph} , with an average energy per photon, \bar{E} , we compute the momentum input per time caused by RP from UV radiation in the following way:

$$\dot{\mathbf{P}}_{\text{UV, dust}} = \sigma_{\text{d}} n \frac{\bar{E}_{\text{ph}}}{c} \dot{N}_{\text{ph}} dV, \quad (\text{C1})$$

$$\dot{\mathbf{P}}_{\text{UV, H}} = \sigma_{\text{H}} n_{\text{H}} \frac{\bar{E}_{\text{ph}}}{c} \dot{N}_{\text{ph}} dV, \quad (\text{C2})$$

$$\dot{\mathbf{P}}_{\text{UV, H}^+} = n^2 \frac{\bar{E}_{\text{ph}}}{c} \dot{N}_{\text{ph}} dV, \quad (\text{C3})$$

where $\dot{\mathbf{P}}_{\text{UV, dust}}$, $\dot{\mathbf{P}}_{\text{UV, H}}$ and $\dot{\mathbf{P}}_{\text{UV, H}^+}$ are the momentum deposition per unit time on dust, atomic hydrogen and ionized hydrogen, respectively. The quantities σ_{H} , \bar{E}_{ph} , \dot{N}_{ph} are the hydrogen cross section, the mean energy per photon and the incoming photons per unit time per unit area, respectively.

APPENDIX D: EQUATIONS FOR HEATING AND COOLING OF DUST

The gas-dust coupling is given by the following expression [Hollenbach & McKee \(1979\)](#):

$$\Gamma_{\text{dust-gas}} = n n_{\text{dust}} \sigma_{\text{dust}} v_{\text{p}} f 2k_{\text{B}} (T - T_{\text{dust}}), \quad (\text{D1})$$

where n and n_{dust} are the number density of gas and dust, σ_{dust} is the dust cross section and v_{p} is the thermal speed of protons for a given temperature T . f corrects the coupling strength for different ionization fractions and temperatures.

We compute the heating by the interstellar radiation field with the following equation ([Bakes & Tielens 1994](#)):

$$\Gamma_{\text{pe}} = 10^{-24} \epsilon_{\text{pe}} G_0 n_{\text{H}} \text{ erg s}^{-1} \text{ cm}^{-3}, \quad (\text{D2})$$

where G_0 is the flux normalized to the Habing field for the solar neighborhood and ϵ_{pe} is the photoelectric heating efficiency and n_{H} is the hydrogen number density. ϵ_{pe} is given by eq. 43 of [Bakes & Tielens \(1994\)](#).

The H_2 formation heating is calculated as such ([Glover & Mac Low 2007](#))

$$\Gamma_{\text{H}_2} = 7.2 \times 10^{-12} \frac{R_{\text{H}_2}}{1 + n_{\text{cr}}/n} \text{ erg s}^{-1} \text{ cm}^{-3}, \quad (\text{D3})$$

where R_{H_2} measures the rate of H_2 formation on dust grains and n_{cr} is the critical density given by

$$\frac{1}{n_{\text{cr}}} = \frac{x_{\text{H}}}{n_{\text{cr,H}}} + \frac{x_{\text{H}_2}}{n_{\text{cr,H}_2}}. \quad (\text{D4})$$

x_{H} and x_{H_2} are the abundances of atomic and molecular hydrogen. As discussed by ([Glover & Mac Low 2007](#)) we take the values for x_{H} from [Lepp & Shull \(1983\)](#) with the modification from [Martin et al. \(1996\)](#) and the value for x_{H_2} from [Shapiro & Kang \(1987\)](#).

APPENDIX E: ADDITIONAL FIGURES: DUST CHEMISTRY

We show the corresponding molecular hydrogen fraction, $f_{\text{H}_2} = 2n_{\text{H}_2}/(n_{\text{H}^+} + n_{\text{H}} + 2n_{\text{H}_2})$, vs. time in Fig. E1. The formation timescale of H_2 is given by $T_{\text{H}_2} = 1 \text{ Gyr}/(n_{\text{H}}/\text{cm}^{-3})$

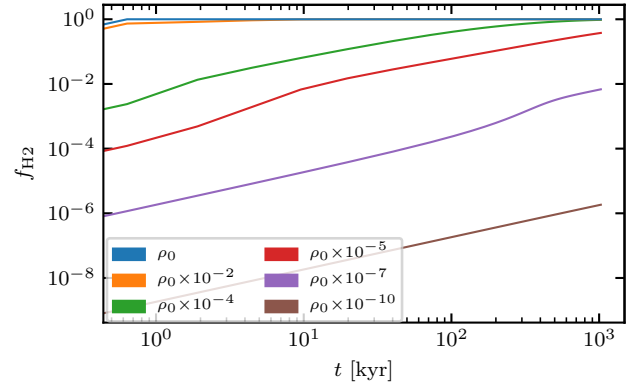


Figure E1. Molecular hydrogen fraction vs. time for dust chemistry setup in §5.3. The different lines show different densities used for the dust chemistry setup. Higher densities form molecular hydrogen faster than lower ones.

and for the density ρ_0 it is roughly 1 yr. We can see that both the blue and orange line of Fig. E1 complete the formation of H_2 well within the simulated time period.

APPENDIX F: ADDITIONAL FIGURES: STAR FORMING SETUP

Fig. F1 shows the emitted energy rate at a given wavelength for a stellar particle modeled according to §3.1. Everything to the left of the Lyman-continuum is left of the blue vertical line and emitted in the ionizing band. Everything to the right of the blue line is emitted in the non-ionising band. Although the hot spot accretion is emitted from a smaller area it dominates in the bolometric luminosity output due to its higher temperature (see fig. 9 upper right panel). γ is the fraction that is emitted in the ionising regime from the total luminosity output.

APPENDIX G: RADIATION PRESSURE ACTING ON THE INTERIOR OF HII REGIONS

In this section we apply our scheme to the scenario of dusty HII regions and see if the scheme is producing expected outcomes. The work by [Draine \(2011\)](#) provides semi-analytical descriptions for such cases and we will use these as a reference.

[Draine \(2011\)](#) describe the interior of dusty HII regions in static equilibrium based on the following equation

$$n\sigma_d \frac{L_{\text{n}} e^{-\tau} + L_{\text{i}} \Phi(r)}{4\pi r^2 c} + \alpha_{\text{B}} n^2 \frac{\langle h\nu \rangle_{\text{i}}}{c} - \frac{d}{dr} (2nk_{\text{B}}T) = 0, \quad (\text{G1})$$

where n , σ_{d} , L_{n} , L_{i} , τ and $\Phi(r)$ are the proton density, dust opacity, neutral and ionizing luminosity, the optical depth and extinction of ionizing radiation, respectively. The quantity $\langle h\nu \rangle_{\text{i}}$ is the mean energy of a photon which is 18 eV in our case and r measures the radial distance from the source of ionizing photons. Eq. G1 assumes a constant dust to gas ratio everywhere and takes into account the radiation pressure on dust by ionizing and non-ionizing radiation (first term) and radiation pressure on gas by ionizing radiation

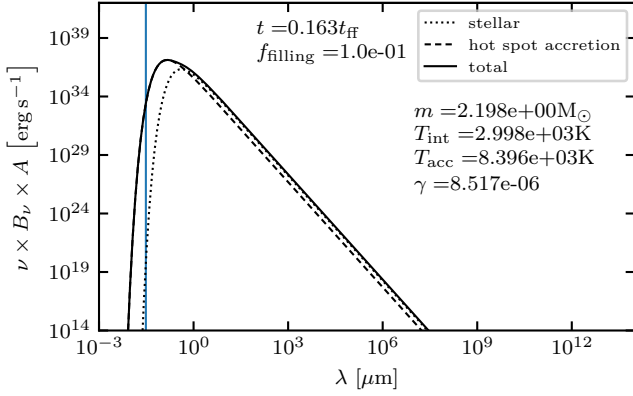


Figure F1. Stellar spectrum of the primary stellar particle at simulation time t . The y-axis is the resulting product of frequency, ν , Planck's law, B_ν , and the respective area from which the radiation is emitted, A . In the case of hot spot accretion we assume that the emission originates from f_{filling} times the area of the stellar object. The dotted line shows the purely stellar component and the dashed line shows the component due to hot spot accretion. The sum of both components is shown by the solid line. T_{int} and T_{acc} are calculated based on eq. 14 and eq. 15, respectively. γ is the fraction of the power that is emitted in the ionising regime from both the internal and accretion luminosity combined (see eq. 16).

(second term). Radiation pressure is opposed by thermal pressure (third term) which governs the static equilibrium.

Fig. G1 shows both semi-analytic predictions based on the work of Draine (2011) in dotted lines and the result from our code in solid line. While our solution has not reached its steady state, it matches the semi-analytic prediction (in-between red and purple dotted lines; $10^3 < Q_0 n_{\text{rms}} < 10^4$; for $\gamma = 20$). The spikes are minor waves in the density field which is still adjusting for true static equilibrium. The different semi-analytic solutions are categorized based on the product of the number of ionising photons per second normalized to 10^{49} s^{-1} and the root mean square number density, which are labeled Q_0 and n_{rms} , respectively. The latter is calculated in the following way according to the work of Draine (2011)

$$n_{\text{rms}} = n_0 \left(\frac{3}{y_{\text{max}}^3} \int_0^{y_{\text{max}}} \frac{1}{u^2} y^2 dy \right)^{1/2}, \quad (\text{G2})$$

where n_0 is the characteristic density scale,

$$n_0 = \frac{4\pi\alpha_B}{Q_0} \left(\frac{2ckT}{\alpha_B \langle h\nu \rangle} \right)^3. \quad (\text{G3})$$

The dimensionless quantities u and y refer to the density and length scale

$$u = \frac{n_0}{n} \quad (\text{G4})$$

$$y = \frac{r}{\lambda_0} \quad (\text{G5})$$

with λ_0 being the characteristic length scale defined as

$$\lambda_0 = \frac{Q_0}{4\pi\alpha_B} \left(\frac{\alpha_B \langle h\nu \rangle}{2ckT} \right)^2. \quad (\text{G6})$$

Further the quantity γ is calculated in the following way

$$\gamma = \left(\frac{2ckT}{\alpha_B \langle h\nu \rangle} \right) \sigma_d, \quad (\text{G7})$$

where our value of γ is roughly 15. The quantity γ refers to the dust opacity towards ionizing radiation. Note that we do not employ a constant dust opacity for non ionizing radiation in our scheme, which is a significant difference to the assumptions made by Draine (2011). Our dust opacity for ionizing radiation however is constant, namely $\sigma_d = 1.5 \times 10^{-21} \text{ cm}^2 \text{ H}^{-1}$. Our setup compares to the setup $10^3 < Q_0 n_{\text{rms}} < 10^4$ and features $\gamma \approx 15$. We can see that our solution recovers features of both the purple and red dotted line.

This paper has been typeset from a \LaTeX file prepared by the author.

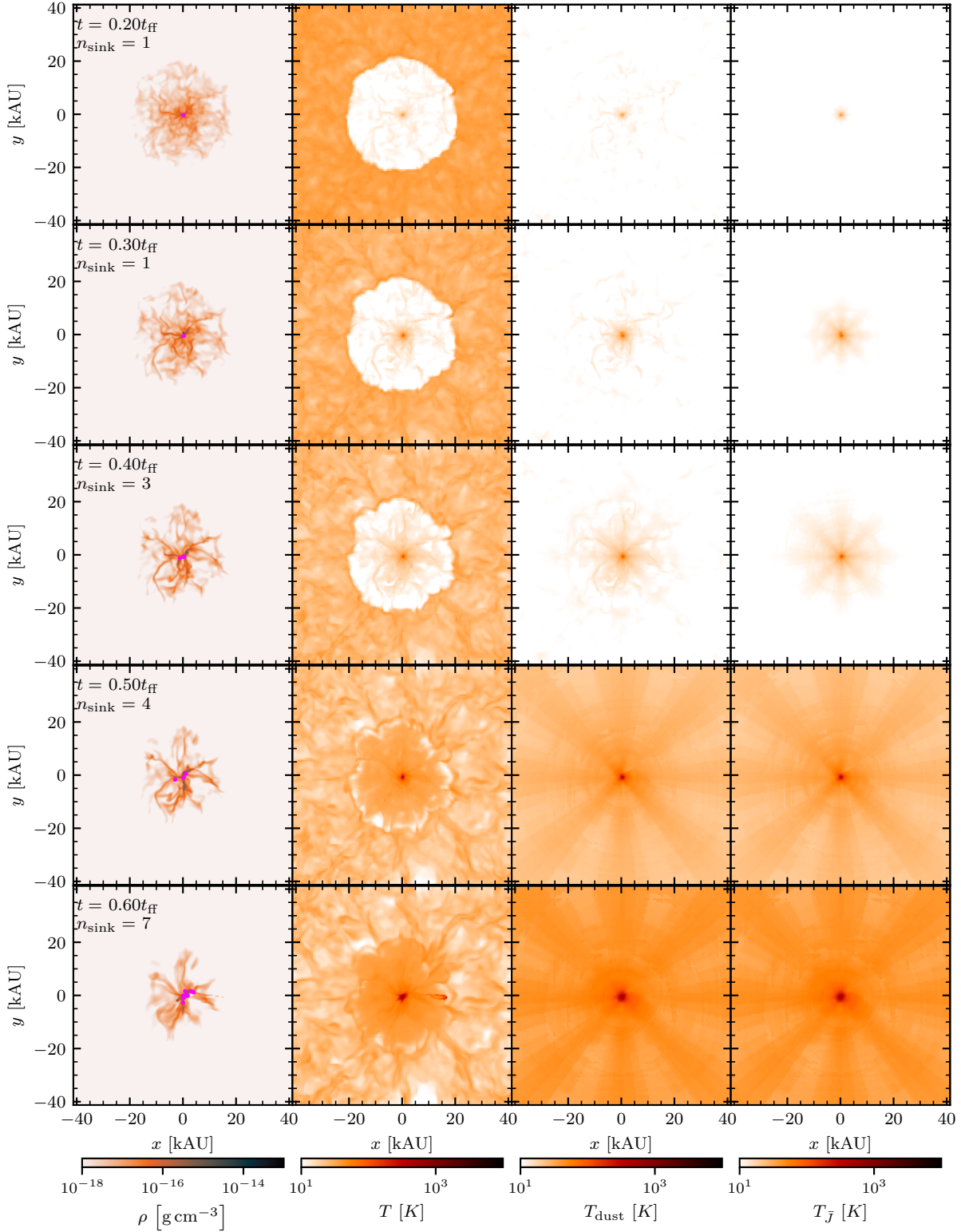


Figure F2. Slices through $z = 0$. Organized in rows we show from left to right density, gas temperature, dust temperature and radiation temperature across different times. The time, t , is measured in free-fall times, $t_{\text{ff}} = 42.3 \text{ kyr}$. The number of sink particles present is labeled n_{sink} . This figure pertains to the SF core setup of §7.

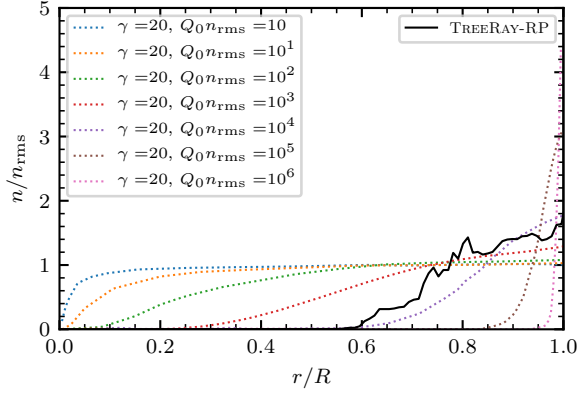


Figure G1. Radial profile showing the interior of an HII region taking into account radiation pressure. The plot shows the number density vs. radial distance. The solid line shows the curve obtained from our code and the dotted lines show semi-analytic models from [Draine \(2011\)](#) (see their Fig. 2).